DOI: 10.26599/FSHW.2025.9250900

Contents lists available at SciOpen

Food Science and Human Wellness

journal homepage: https://www.sciopen.com/journal/2097-0765

China Food Publishing Co.

Chemical Proteomics-Based Reactive Metabolites and Protein Adducts: The New Perspective on the Metabolism of Food Furanocoumarins

Zhendong Wang[1, a], Shan Han[1, a], Xueyi Cai[1], Meng Li[2], Jingrui Qian[1], Qiyao Jiang[1], Xiqing Bian[3]*, Jian-Lin Wu[4]*, Yue Zhuo[1]*

[1] *Science and Technology Innovation Center, Guangzhou University of Chinese Medicine, Guangzhou, 510405, China*

[2] *College of Food and Health, Guangzhou City Polytechnic, Guangzhou, 511370, China*

[3] *School of Pharmacy, Macau University of Science and Technology, Taipa, Macao SAR, 999078, China*

[4] *State Key Laboratory for Mechanism and Quality of Chinese Medicine, Macau University of Science and Technology, Avenida Wai Long, Taipa, Macau SAR, 999078, China*

ABSTRACT: Furanocoumarins are widely found in various foods and exhibit a range of biological activities. However, due to the structural characteristics of their furan ring, they are susceptible to being metabolized by cytochrome P450 enzymes, thereby forming reactive metabolites (RMs), leading to a dual effect: firstly, the inhibition of CYP enzyme activity, which may result in food-drug interactions affecting drug absorption; and secondly, the formation of covalent bonds between RMs and proteins, potentially disrupting protein function and causing toxicity. Consequently, understanding the metabolic metabolism of furanocoumarins in biological systems is essential for ensuring food safety. This study employed chemical proteomics-based RMs and protein adducts analytical approach to investigate mechanisms of psoralen (PRN), a representative simple-structured furanocoumarin. Initially, dose-dependent hepatotoxicity was confirmed in mice treated with excessive PRN exposure. Subsequently, an LC-MS strategy was developed to identify PRN RM-protein adducts both *in vitro* (liver microsomes) and *in vivo* (mouse liver). The abundance of PRN RM-protein adducts was positively correlated with the severity of liver injury. Further analysis identified CYP2C6, CYP3A1, CYP2E1, and CYP2A3 as the primary enzymes facilitating the formation of PRN RM-protein adducts. Finally, label-free quantitative proteomics, integrated with network pharmacology, indicated that disruption of glutathione metabolism may be a potential hepatotoxic pathway activated by PRN RM-protein adducts. This study provides new insights into the dual role of furanocoumarin-induced food-drug interactions and hepatotoxicity, establishes a methodological framework for assessing food safety, and offers critical insights for their judicious application.

Key Words: Furanocoumarins; Reactive metabolites; Psoralen; Protein adducts; Hepatotoxic.

1. Introduction

Furanocoumarins, a class of naturally occurring coumarin derivatives, are widely distributed in various plant families, including citrus fruits, *Umbelliferae* vegetables, as well as species from *Rutaceae*, *Moraceae*, and

[a] These authors contributed equally to this work and should be considered co-first authors.
***Corresponding author**
Xiqing Bian, xqbian@must.edu.mo; Jian-Lin Wu, jlwu@must.edu.mo; Yue Zhuo, zhuoyue@gzucm.edu.cn.

Received 8 October 2025
Received in revised from 4 November 2025
Accepted 24 November 2025

Leguminosae [1-3]. Traditionally, these plants have been recognized for their diverse functional properties, such as anti-toxic, anti-oxidative, appetizer, bone health promoting, stomach anti-inflammatory, and cardiac effects [4, 5]. Structurally, furanocoumarins consist of a furan ring fused to a coumarin backbone at either the C6–C7 (linear type) or C7–C8 (angular type) positions. Their biological activity is highly dependent on this structural arrangement—specifically, the orientation of the furan ring, the coumarin core, and the type, position, and number of substituents[6].

Upon dietary intake, furanocoumarins are rapidly absorbed and metabolized primarily via cytochrome P450 enzymes (P450) [7, 8], the oxidation of the furan double bond can generate reactive intermediates such as furan epoxides or γ-ketoenals[9, 10]. These electrophilic metabolites form covalent adducts with amino acid residues (e.g., cysteine, lysine) and glutathione, leading to mechanism-based inhibition of CYP enzymes—particularly CYP3A4—and disruption of protein function. This inhibition underlies clinically significant drug interactions; for example, furanocoumarin-rich grapefruit juice irreversibly inhibits CYP3A4, reducing fexofenadine absorption by 28% and increasing systemic exposure of drugs like simvastatin by over 700% [11, 12]. Despite their widespread dietary occurrence, furanocoumarins exhibit substantial variability in bioactivity and toxicity, highlighting the need to identify specific protein targets linked to hepatotoxicity and to clarify the role of reactive metabolite-protein adducts in liver injury. Consequently, profiling these metabolites is essential for assessing food-drug interactions and improving safety screening[13].

The identifying of relevant modified protein targets represents a critical challenge [14] in understanding furanocoumarins-drug interactions and hepatotoxicity. Currently, common methods for identifying covalently modified proteins include using radiolabeled drugs [15] and antigen-antibody immunopurification approaches [16]. However, these techniques have several limitations, such as low specificity, complex procedures, high costs, and the inability to identify multiple targets simultaneously [17] .While activity-based protein profiling (ABPP) offers improved screening capacity, its reliance on structurally modified probes may alter compound metabolism and limit applicability to unstable RMs [18]. To overcome these issues, our laboratory has developed an innovative high-throughput screening strategy enabling specific identification of modified proteins without structural derivatization, successfully applied to study protein modifications induced by various phytotoxins toosendanin [19, 20], diosbulbin B [21], and osthole [22].

Psoralen (PRN) is a typical simple-structured furanocoumarin compound that is commonly found in a variety of plants and has demonstrated considerable medicinal potential[23]. However, excessive PRN exposure can also cause toxicity, especially liver toxicity, which somewhat limits its application [24, 25]. PRN is classified as a coumarin compound that contains a furan ring and an α, β-unsaturated lactone ring [25, 26]. These structural features are the active functional groups capable of generating RMs via the action of P450 [27]. Previous research has demonstrated that PRN-induced hepatotoxicity is associated with PRN-derived RMs. Specifically, PRN undergoes oxidation by cytochrome P450 enzymes to form reactive furan epoxides or γ-ketoaldehyde intermediates, resulting in mechanism-based inhibition of CYP3A4 [28]. Additionally, PRN has the capacity to directly attach to CYP3A4, CYP2D6, GST-μ and GST-α, hindering their enzymatic

activities and causing a depletion in GSH levels, which ultimately contributes to liver damage [25]. This effect is attributed to the distinctive structure of its furan ring or α, β-unsaturated lactone, which facilitates its binding affinity to target proteins [25, 29].

In this study, PRN was utilized as a representative furanocoumarin to comprehensively investigate its metabolic activity both in vitro and in vivo, as well as the mechanisms of hepatotoxicity mediated by RMs, employing an integrated experimental approach. Initially, we characterized the metabolic pathways of PRN and the formation of RM-amino acid adducts using liquid chromatography -mass spectrometry (LC-MS) and a chemical proteomics-based approach to identify RMs and protein adducts, supplemented by cytochrome P450 (CYP) inhibition assays to determine the primary metabolic enzymes involved. Subsequently, dose-dependent hepatotoxicity was assessed in murine models through biochemical and histopathological evaluations following overdose administration [30, 31]. *In vivo* validation confirmed the presence of RM adducts in hepatic tissue, which correlated with the severity of toxicity. Finally, proteomics combined with pathway analysis (KEGG/GO) was employed to identify critical protein targets and elucidate the hepatotoxic mechanisms associated with the formation of PRN RM-protein adducts. This study provides novel insights into the metabolic profile of furanocoumarins and their potential toxicity mechanisms.

2. Materials and Methods

2.1 Chemicals and reagents

PRN (purity 98%), sulfaphenazole (purity 99%), ketoconazole (purity 98%) and pronase E (PE) were obtained from yuanye Bio-Technology Co., Ltd in Shanghai, China). Formic acid (FA), Ammonium bicarbonate (NH_4HCO_3), Calcium chloride anhydrous ($CaCl_2$), ticlopidine (purity 97%), quinidine (purity 98%), disulfiram (purity 97%), methoxsalen (purity 99%), potassium phosphate monobasic, and potassium phosphate dibasic anhydrous were supplied from Macklin Biochemical Co.,Ltd in Shanghai, China. A-naphthoflavone (purity 98%) was sourced from Shanghai Aladdin Biochemical Technology Co., Ltd (Shanghai, China), Thermo Fisher Scientific, located in Waltham, MA, USA, supplied the rat liver microsomes. L-Glutathione reduced (GSH), N-acetyl lysine (NAL), N-acetyl cysteine (NAC), IAA (Iodoacetamide) Dithiothreitol (DTT) and α-chymotrypsin (α-C) were purchased from SigmaAldrich (MO, USA). Nicotinamide adenine dinucleotide phosphate (NADPH) generating system consists of solutions A and B (NADPH-A & B), supplied by Corning Incorporated in New York, USA. C18 solid-phase extraction (SPE) columns (Waters Corp., USA). Ultrapure water was produced using the RODI-220A system manufactured by Guangzhou Ewell Biotechnology Co., Ltd, located in Guangzhou, China. Anaqua Chemicals Supply Inc., Ltd (Houston, TX) provided acetonitrile (CAN, HPLC grade). Alanine Aminotransferase (ALT) assay kit, Aspartate Aminotransferase (AST) assay kit, Malondialdehyde (MDA) assay kit, Superoxide Dismutase (SOD) assay kit, and Glutathione (GSH) assay kit (Nanjing Jiancheng Bioengineering Institute); Catalase (CAT) assay kit and Bradford Protein Concentration Determination Kit (Shanghai Beyotime Biotechnology Co., Ltd.); Glutathione S - transferase (GST) assay kit (Shanghai Dibo Biotechnology Co., Ltd.).

2.2 Incubation of PRN and Amino acids (AAs) / GSH in rat liver microsomes

The water bath was preheated to 37 ℃, and liver microsomes, NADPH-A, NADPH-B, PRN, GSH, NAL, and NAC were thawed on ice. Firstly, 80 μL of 0.5 M PBS buffer (pH=7.4), 3.7 μL of PRN (to achieve a final concentration of 50 μmol/L), 20 μL of cofactor NADPH-A, and 4 μL of cofactor NADPH-B were sequentially added to a centrifuge tube. Subsequently, 8 μL of 0.25 M GSH, NAC, NAL solution (final concentration of 5.0 mmol/L), and 272.3 μL of ultrapure water were added. The combination was then preheated at 37 ℃ for a period of 2 minutes. After preheating, 20 μL of liver microsomes (to achieve a 1 mg/mL concentration in the final solution) was added to initiate the reaction. The incubation system was maintained at a constant temperature of 37 ℃, with a total reaction volume of 400 μL. At 0 minutes and 120 minutes, 180 μL of reaction mixture was obtained from each time point, and the reaction was stopped by adding 4 volumes of ice-cold acetone and placing the samples on ice. At 4 ℃, the tubes were then centrifuged at 15,000 g for 10 minutes. After centrifugation, 750 μL of the supernatant was dried using a nitrogen stream. The residue was then reconstituted in a 50% methanol solution for 100 μL. For analysis, 90 μL of the supernatant was introduced into an Ultra Performance Liquid Chromatography system combined with Liquid Chromatography Quadrupole-Time of Flight Mass Spectrometry (UPLC-Q-TOF-MS/MS).

2.3 P450 Metabolizing Enzyme Inhibition Studies

To explore which specific P450 enzymes [32] are responsible for producing reactive metabolites of PRN, seven P450 inhibitors were evaluated. Based on literature references and preliminary dose-response experiments, the concentration of the inhibitor was finally selected as: ketoconazole (1.0 μmol/L for CYP3A1), sulfaphenazole (20 μmol/L for CYP2C6), α-naphthoflavone (1.0 μmol/L for CYP1A2), ticlopidine (100 μmol/L for CYP2C11), quinidine (5.0 μmol/L for CYP2D1), disulfiram (100 μmol/L for CYP2E1), and methoxsalen (20 μmol/L for CYP2A3) [33]. Incubation mixtures contained 0.5 M potassium phosphate buffer (pH 7.4), 20 μmol/L PRN, 1.0 mmol/L NADPH, 1.0 mmol/L GSH, and the respective inhibitors at their specified concentrations. Controls containing no chemical inhibitors were included. The mixtures were initially incubated in a 37 ℃ water bath for 2 minutes before adding RLM (20 mg/mL) to initiate metabolic reaction, and then diluted to a final 1 mg/mL concentration, resulting in a total incubation volume of 400 μL. At 0 and 120 minutes, reaction mixture of 180 μL was collected, terminated by adding ice-cold acetonitrile of four volumes. After centrifuging the samples at 12,000 g for 10 minutes at 4 ℃, 900 μL of the supernatants were dried using nitrogen. The dried samples were re-dissolved in 100 μL of 50% methanol containing 20 μmol/L ferulic acid as an internal standard, centrifuged again, and 90 μL portion of the supernatant was introduced into an LC-MS system.

2.4 Animals

Male Kunming (KM) mice (4-6 weeks, 18-22 g) were sourced in Guangzhou University of Chinese medicine, under certificate number SYXK 2018-001, then housed in a pathogen-free animal lab, with a 12-hour light/dark cycle and a temperature maintained at (22 ± 4) ℃, and they had unrestricted access to food and water. The researchers strictly complied with the animal welfare guidelines and ethical norms provided by the Experimental Animal Center of Guangzhou University of Chinese Medicine. This study was reviewed by

the Animal Experimental Ethics Committee of Guangzhou University of Traditional Chinese Medicine on April 26, 2023 (Ethics Number 20230426002). Mice were organized into 4 groups (n=6): Group 1 received orally administered of 0.5% CMC-Na for 4 consecutive days, Group 2-4, the mice were orally administered with 40, 160, or 320 mg/kg of PRN and vehicle (0.5% CMC-Na) for 4 consecutive days, doses and routes of administration were chosen according to prior references [25, 31]. This design includes a low dose (40 mg/kg) at the Lowest Observable Adverse Effect Level (LOAEL) to observe early effects, a mid-dose (160 mg/kg) that reliably induces toxicity, and a high dose (320 mg/kg) that produces severe injury. This non-linear spacing was crucial for capturing a wide dynamic range of biological responses, which is essential for correlating reactive metabolite adduct formation with the progression of pathological outcomes.

2.5 Preparing samples for analysis of liver and blood

Blood samples were collected from each group of mice by ocular enucleation. After collection, plasma samples were allowed to sit for 2 hours and then centrifuged at 4 ℃ and 3000 g for 10 mins to obtain the supernatant. Following blood drawing, mouse livers were perfused with saline. Liver tissue sections were preserved in neutral buffered formalin, encased in paraffin, sliced into sections, and stained using hematoxylin and eosin (H&E). The remaining liver tissues were maintained at a temperature of -80 ℃. The serum was used for subsequent assays of ALT and AST, and liver tissues were used for subsequent assays of MDA, SOD, GSH, CAT, and GST.

Liver tissue (0.1g) was homogenized in 1 mL of 0.5 M PBS buffer (pH=7.4), then centrifuged to remove debris (9, 000 g, 10 min, 4 ℃). The supernatant was combined with cold acetone in a 1:4 ratio to precipitate the protein, then centrifuged at 10, 000 g and 4 ℃ for 5 min. The supernatant was gathered and evaporated under nitrogen, and then redissolved in 100ul methanol (50 %), then centrifuged at 15000 g, 4 ℃ for 10 min, and 90 ul was injected into the injection vial for the identification of PRN RMs and PRN RM-AAs adducts *in vivo*.

2.6 Protein digestion

Protein precipitates were dissolved in 8 M urea and quantified using the Beyotime Bradford Protein Assay Kit following the manufacturer's protocol. For tryptic digestion: 100 μg protein sample was diluted to 100 μL with ultrapure water and subjected to sequential reduction and alkylation. First, 5 μL of 200 mmol/L dithiothreitol (DTT) was added followed by 1 h incubation at room temperature. Subsequently, 4 μL of 1 M iodoacetamide (IAA) was introduced and the mixture was incubated in darkness for 1 h at ambient temperature. The alkylation reaction was quenched by adding 20 μL of 200 mmol/L DTT with additional 1 h incubation. The urea concentration was adjusted to 0.8 M using 25 mmol/L ammonium bicarbonate (NH_4HCO_3), followed by addition of 2 μg sequencing-grade trypsin (1 mg/mL in 1% acetic acid). Enzymatic digestion proceeded for 12 h at 37℃ in a temperature-controlled water bath.

Digested peptides were purified using C18 SPE columns with the following protocol: Columns were pre-equilibrated with six column volumes of 0.1% trifluoroacetic acid (TFA) in acetonitrile (ACN) followed by six volumes of 0.1% TFA in ultrapure water. The sample was then diluted to 1 mL with 0.1% TFA in

ultrapure water and loaded onto a SPE columns and washed with 1 mL of 0.1% TFA aqueous solution. Bound peptides were eluted with 200 μL of 0.1% TFA in 70% ACN. Eluates were concentrated to dryness under nitrogen stream and reconstituted in 50 μL of 2% ACN containing 0.1% TFA. After centrifugation at 15,000 × g for 10 min, supernatants were transferred to LC-MS vials for analysis.

2.7 UHPLC-Q-TOF-MS/MS analysis for metabolic profiling

An Agilent 1290 infinity UHPLC system (California, U.S.A.) with a binary pump, an autosampler, and a thermostated column compartment coupled with 6545XT Q-TOF-MS system (California, U.S.A.) was used for the identification of PRN RMs and PRN RM-AAs adducts. They were separated using an Agilent ZORBAX Eclipse Plus C18 column with length of 2.1 mm × 50 mm, 1.8 μm particle size (Agilent, California, U.S.A.). The mobile phase included phase A, containing double distilled H_2O with 0.1% FA, and phase B, which was ACN with 0.1% FA. The linear gradient elution was maintained as follows: 5% B in 0-0.5 min, 5%-10% B in 0.5-3 min, 10%-30% B in 3-10 min, 30%-60% B in 10-15 min, 60%-100% B in 15-18 min, 100% B in 18-21 min, 100%-5% B in 21-21.1 min, flowing at 0.35 mL/min. The column temperature was operated at a temperature of 35 ℃ with an injection volume of 2 μL. The temperatures of dry gas and sheath gas were set at 320 and 400℃, with respective flow rates of 10 and 12 L/min. The nebulizer operated at 45 psi, with the capillary and nozzle voltages set to 4000 V and 500 V, respectively, for positive ESI mode. The fragmentor was adjusted to 180 V, and the collision energy was set to 30 eV. Mass spectrometry data were gathered in centroid mode across an m/z range of 100-1700. Finally, all data were processed using Agilent MassHunter Qualitative Analysis B.10.

2.8 Chemical proteomics analysis

Chromatographic separation was performed using an Easy-nanoLC 1200 system (Thermo Scientific™) coupled to an Orbitrap Fusion™ Tribrid™ mass spectrometer (Thermo Scientific™). Peptides were loaded onto a C18 analytical column (75 μm × 20 cm, 1.9 μm particles, 120 Å pore size) at a constant flow rate of 300 nL/min. The mobile phases consisted of (A) 0.1% FA in water and (B) 0.1% FA in 80% ACN. A linear gradient was applied as follows: 4%–8% B (0–5 min), 8%–28% B (5–95 min), 28%–38% B (95–111 min), 38%–100% B (111–115 min), and 100% B (115–120 min), with an injection volume of 3 μL.

Mass spectrometric analysis was conducted in positive-ion mode using an EasySpray ion source. Full-scan MS spectra (350–1500 m/z) were acquired in the Orbitrap at a resolution of 60,000 (maximum injection time: 50 ms). Data-dependent MS/MS acquisition selected the top 10 most intense precursor ions (charge states 2–6) for higher-energy collisional dissociation (HCD) fragmentation (maximum injection time: 75 ms). Instrument performance was validated daily using a HeLa cell digest standard (Thermo Scientific™).

The raw MS data acquired from the Orbitrap Fusion mass spectrometer were processed using Proteome Discoverer software (version 2.5). MS/MS spectra were searched against the UniProtKB Mouse complete proteome database (release 2022_03, 85,965 entries) using trypsin specificity, allowing up to two missed cleavages. The search included variable modifications of carbamidomethylation (C), oxidation (M), and N-terminal acetylation, along with PRN-related variable modifications: $C_{11}H_4O_5$ and $C_{11}H_6O_4$ on lysine (K),

and $C_{11}H_4O_3$, $C_{11}H_4O_4$, $C_{11}H_6O_4$, $C_{11}H_6O_5$, $C_{11}H_8O_5$, $C_{11}H_8O_4$, on cysteine (C) residues. Precursor ion and fragment ion mass tolerances of were set to 10 ppm and 0.02 Da, respectively. Peptide spectral matches (PSMs) were filtered at a 1% false discovery rate (FDR) threshold. The mass spectrometry proteomics data have been deposited to the ProteomeXchange Consortium via the PRIDE partner repository with the dataset identifier PXD064256.

2.9 Label-Free quantitative proteomics

Raw mass spectrometry data were processed using Proteome Discoverer 2.5 (Thermo Scientific). MS/MS spectra were searched against the UniProtKB database (release 2023_10) using trypsin digestion specificity, allowing a maximum of two missed cleavages. Fixed modifications included carbamidomethylation (C), while variable modifications comprised methionine oxidation (M) and N-terminal acetylation (with a maximum of three variable modifications permitted per peptide). Label-free quantification (LFQ) was performed using the intensity-based absolute quantification (iBAQ) algorithm with match-between-runs enabled. Peptide and protein identifications were filtered at a 1% false discovery rate (FDR) using the Percolator algorithm.

Differentially expressed proteins (DEPs) between control and PRN-treated groups were identified based on significant protein abundance changes, defined by thresholds of | log2 (fold change) | > 1 and $P < 0.05$. These DEPs were subsequently subjected to enrichment analyses. Statistical analysis and volcano plot generation were performed using GraphPad Prism 9.3.

Gene Ontology (GO) enrichment analysis was conducted using Fisher's exact test with Benjamini-Hochberg correction for multiple hypothesis testing. Hierarchical clustering heatmaps were constructed with TBtools 2.0, employing Euclidean distance and complete linkage methods. GO (Gene Ontology) and KEGG (Kyoto Encyclopedia of Genes and Genomes) enrichment analyses were performed on modified proteins and differentially expressed proteins (DEPs) using Metascape (https://metascape.org/gp/index.html#/main/step1), with pathway construction restricted to the Mus musculus species. Visualization of enrichment results was conducted via the Weishengxin online platform (https://www.bioinformatics.com.cn/).

3. Results

3.1 Analysis of PRN metabolism in vitro

Existing research has shown that PRN is prone to generating RMs [28]. Therefore, an *in vitro* incubation experiment was first conducted using RLM to investigate the metabolism of PRN (M0). The results displayed that PRN (Fig.S1) at the retention times of 9.03 min had an $[M+H]^+$ ion at m/z 187.0390, which matches the formula of $C_{11}H_6O_3$. After 2 hours of incubation in microsomal, six metabolites M1-M6 of PRN were detected (Table1). M1 (Fig.1A) at the retention times of 8.08 min had an $[M+H]^+$ ion at m/z 203.0339, which was 16 Da (15.9949 Da) higher than that of the protonated parent compound, indicating the introduction of an oxygen atom into the molecule. The product ions at m/z 175 $[M+H\text{-}CO]^+$, 159 $[M+H\text{-}CO_2]^+$, and 147 $[M+H\text{-}2CO]^+$

were observed in the high-resolution mass spectrum, further indicated that M1 was $C_{11}H_6O_4$. M2 (Fig.1B) at the retention times of 4.80 min had an $[M+H]^+$ ion at m/z 205.0495, which matches the formula of $C_{11}H_8O_4$. It indicates the addition of a H_2O molecule to PRN ($C_{11}H_6O_3$). The fragmentation ions at m/z 177 $[M+H-CO]^+$, 149 $[M+H-2CO]^+$, and 131 $[M+H-2CO-H_2O]^+$ further indicated that it was $C_{11}H_8O_4$. The metabolite M3(Fig.1C) possesses an [M+H]+ ion of 207 Da at the retention times of 4.77 min, which matches the formula of $C_{11}H_{10}O_4$, indicating the addition of a H_2O molecule and two H atoms. The MS/MS spectrum shows the prominent ions at m/z 189 $[M+H-H_2O]^+$, 161 $[M+H-H_2O-CO]^+$, and 133 $[M+H-2CO-H_2O]^+$, which can confirm the hydrogenation and hydrolysis of unsaturated lactone ring. M4 (Fig.1D) at the retention times of 5.02 min, had the molecular ion peak $[M+H]^+$ at m/z 221.0445, which matches the formula of $C_{11}H_8O_5$. M4 produced product ions at m/z 203 $[M+H-H_2O]^+$, 175 $[M+H-CO-H_2O]^+$, and 147 $[M+H-2CO-H_2O]^+$, the MS/MS spectra show that psoralen is converted to a γ-ketoenal or epoxide intermediate, which then reacts to form 6-HCA or dihydrodiol. The result is in accordance with the previous report [34]. M5 (Fig.S2) had the protonated molecular ion peak m/z (223.0601) at retention times of 2.21, suggesting a molecular formula of $C_{11}H_{10}O_5$. M5 showed the product ions at m/z 205 $[M+H-H_2O]^+$, 177 $[M+H-H_2O-CO]^+$, and 149 $[M+H-2CO-H_2O]^+$. M6 (Fig.S3), with a retention time of 1.56 min, displayed an $[M+H]^+$ ion at m/z 237.0394, corresponding to the formula $C_{11}H_8O_6$. This suggests the addition of a H_2O molecule and two O atoms to PRN ($C_{11}H_6O_3$). The high-resolution mass spectrum revealed product ions at m/z 219 $[M+H-H_2O]^+$ and 191 $[M+H-CO-H_2O]^+$, further confirming that it is $C_{11}H_8O_6$.

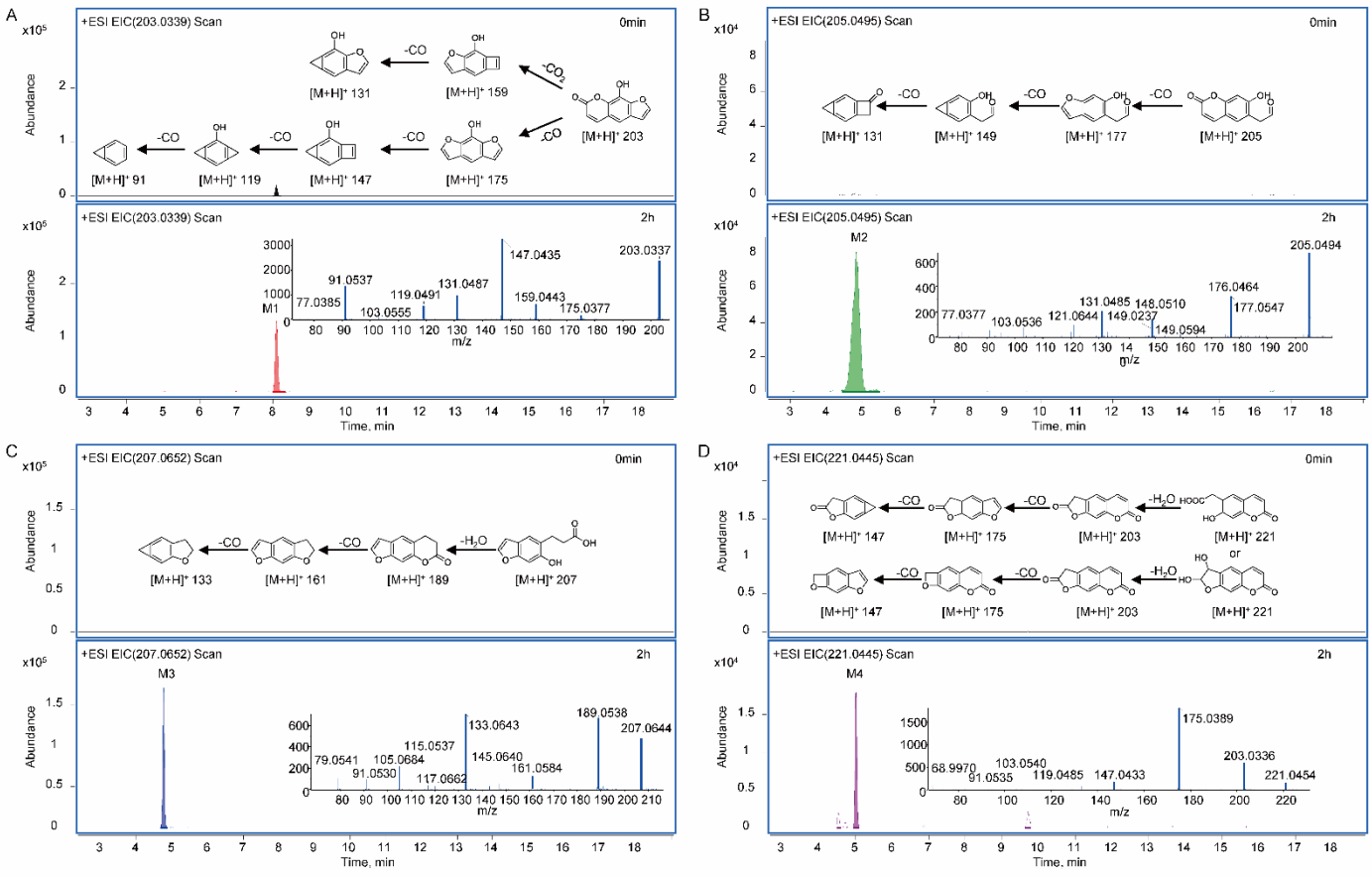

Fig.1 The Extracted ion chromatograms (EICs), possible structure and MS/MS spectrum of M1 (A), M2 (B), M3 (C), M4 (D).

Table 1. Identified metabolites of PRN in RLM.

PRN Metabolite	Retention Time (min)	Molecular Formula	Calculated m/z $[M+H]^+$	Measured m/z $[M+H]^+$	Mass Accuracy (ppm)	Fragment Ion (m/z)
M0	9.03	$C_{11}H_6O_3$	187.0390	187.0386	-2.0	143.0489, 131.0484, 115.0539
M1	8.08	$C_{11}H_6O_4$	203.0339	203.0337	-0.9	175.0377, 159.0443, 147.0435
M2	4.80	$C_{11}H_8O_4$	205.0495	205.0494	-0.7	177.0547, 149.0594, 131.0485
M3	4.77	$C_{11}H_{10}O_4$	207.0652	207.0644	-3.8	189.0538, 161.0584, 133.0643
M4	5.02	$C_{11}H_8O_5$	221.0445	221.0454	4.3	203.0336, 175.0389, 147.0433
M5	2.21	$C_{11}H_{10}O_5$	223.0601	223.0604	1.3	205.0498, 177.0542, 149.0590
M6	1.56	$C_{11}H_8O_6$	237.0394	237.0392	-0.7	219.0282, 191.0345

3.2 Detection of PRN and RMs-AAs conjugates in vitro

Given that PRN can be converted into reactive intermediates, we conducted an investigation into the potential conjugation reactions between PRN and model amino acids. Considering that RMs are typically unstable and only exists for a short period of time, three models AA (GSH, NAC, and NAL) were employed for *in vitro* incubation with PRN to capture these RMs. The results revealed the successful detection of 11 PRN RMs adducts with AAs in positive ion mode (Table 2). The metabolic pathways of PRN RMs in conjunction with GSH, NAC, and NAL are shown in Fig.2.

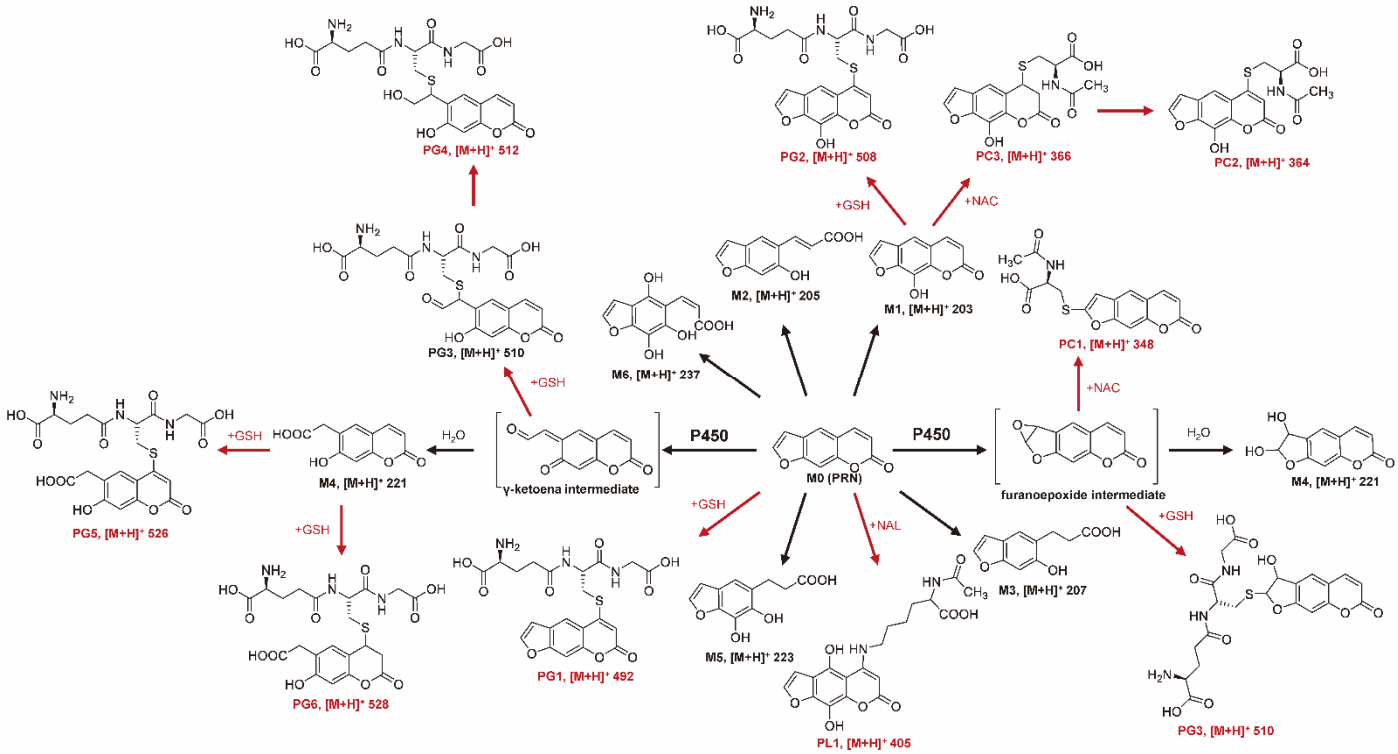

Fig.2 Proposed metabolic pathways of PRN RM Conjugates with GSH, NAC, NAL.

Table 2. PRN RM conjugates formed with amino acids and the modification patterns.

PRN adduct	Substrate	Retention time	Molecular	Calculated m/z $[M+H]^+$	Measured m/z $[M+H]^+$	Mass accuracy (ppm)	Increased mass (Da)	Molecular composition of RM	Modification Type	Biological Source
PC1	NAC	5.19	$C_{16}H_{13}NO_6S$	348.0536	348.0525	-3.3	184	$C_{11}H_4O_3$	P1-C	Microsome
PC2	NAC	8.56	$C_{16}H_{13}NO_7S$	364.0486	364.0463	-6.2	200	$C_{11}H_4O_4$	P2-C	Microsome
PC3	NAC	5.19	$C_{16}H_{15}NO_7S$	366.0642	366.0639	-0.8	202	$C_{11}H_6O_4$	P3-C	Microsome
PL1	NAL	7.30	$C_{19}H_{20}N_2O_8$	405.1292	405.1307	3.6	216	$C_{11}H_4O_5$	P4-K	Microsome
PG1	GSH	6.75	$C_{21}H_{21}N_3O_9S$	492.1071	492.1074	0.5	184	$C_{11}H_4O_3$		Microsome

PG2	GSH	5.61	$C_{21}H_{21}N_3O_{10}S$	508.1020	508.1033	2.5	200	$C_{11}H_4O_4$		Microsome
PG3	GSH	3.39	$C_{21}H_{23}N_3O_{10}S$	510.1177	510.1165	-2.3	202	$C_{11}H_6O_4$		Microsome
PG4	GSH	5.21	$C_{21}H_{25}N_3O_{10}S$	512.1333	512.1331	-0.5	204	$C_{11}H_8O_4$		Microsome
PG5	GSH	3.32	$C_{21}H_{23}N_3O_{11}S$	526.1126	526.1172	8.7	218	$C_{11}H_6O_5$	P5-C	Microsome
PG6-1	GSH	3.15	$C_{21}H_{25}N_3O_{11}S$	528.1283	528.1238	-8.4	220	$C_{11}H_8O_5$	P6-C	Microsome
PG6-2	GSH	3.51	$C_{21}H_{25}N_3O_{11}S$	528.1283	528.1239	-8.3	220	$C_{11}H_8O_5$		Microsome
Pcys1	Cysteine	5.67	$C_{14}H_{11}NO_5S$	306.0431	306.0431	0.1	184	$C_{11}H_4O_3$	P1-C	Liver tissue
Pcys2	Cysteine	4.42	$C_{14}H_{15}NO_6S$	326.0693	326.0695	0.6	204	$C_{11}H_8O_4$	P7-C	Liver tissue
Plys1-1	Lysine	2.95	$C_{17}H_{11}NO_5S$	349.1394	349.1423	8.3	202	$C_{11}H_6O_4$	P3-K	Liver tissue
Plys1-2	Lysine	3.07	$C_{14}H_{11}NO_5S$	349.1394	349.1430	10.3	202	$C_{11}H_6O_4$	P3-K	Liver tissue

Six GSH adducts (PG1-PG6) were identified, with PG2, PG5, and PG6 being reported for the first time in this study. At the retention times of 6.75 min, PG1 (Fig.3A) displayed a molecular ion at m/z 492.1071, corresponding to the formula of $C_{21}H_{21}N_3O_9S$. It is 2H less than the sum of PRN ($C_{11}H_6O_3$) and GSH ($C_{10}H_{17}N_3O_6S$), and the product ions at m/z 417 $[M+H-C_2H_5NO_2]^+$, 345 $[M+H-C_2H_4NO_2-C_2H_3NO_2]^+$ and 260 $[M+H-C_{12}H_7O_3S]^+$ were identified, which further indicated that it was GSH conjugates. PG2 (Fig.3B) and PG3 (Fig.3C) were detected, showing the $[M+H]^+$ signal at m/z 508.1020 and 510.1177, with a chemical formula of $C_{21}H_{21}N_3O_{10}S$ and $C_{21}H_{23}N_3O_{10}S$, respectively. They separated at the retention times of 5.61 min and 3.39 min, respectively. PG2 generated product ions at m/z 490 $[M+H-H_2O]^+$, 379 $[M+H-C_4HO_4-NH_2]^+$ and 203 $[M+H-C_{10}H_{15}N_3O_6S]^+$. PG3 produced product ions at m/z 492 $[M+H-H_2O]^+$, 363 $[M+H-C_5H_7NO_3-H_2O]^+$ and 260 $[M+H-C_{12}H_9O_4S]^+$, which further manifested the conjugate patterns. PG4 (Fig.S4) had a retention time of 5.21 min and displayed a molecular ion at m/z 512.1333, which corresponded to the formula $C_{21}H_{25}N_3O_{10}S$. This indicates that it is 2H and O larger than the combined sum of PRN ($C_{11}H_6O_3$) and GSH ($C_{10}H_{17}N_3O_6S$). The high-resolution mass spectrum detected product ions at m/z 308 $[M+H-C_{11}H_8O_4]^+$, 233 $[M+H-C_9H_{15}N_3O_6-H_2O]^+$ and 205 $[M+H-C_{10}H_{17}N_3O_6S]^+$, which further confirmed it was GSH conjugates. This is the first report of hydrated PRN RM-GSH conjugates. PG5 (Fig.S5), with a retention time of 3.32 min, displayed an $[M+H]^+$ ion at m/z 526.1126, corresponding to the formula $C_{21}H_{23}N_3O_{11}S$. The high-resolution mass spectrum revealed product ions at m/z 508 $[M+H-H_2O]^+$, 379 $[M+H-C_2H_3NO_2- C_2H_4NO_2]^+$ and 219 $[M+H-C_{10}H_{17}N_3O_6S]^+$, further confirming the conjugate pattern. PG6-1 and PG6-2 (Fig.S6) were isomers, had the molecular ion at m/z 528.13, which matches the formula of $C_{21}H_{25}N_3O_{11}S$. They separated at the retention times of 3.15 min and 3.51 min, respectively. The product ions at m/z 510 $[M+H-H_2O]^+$, 492 $[M+H-2H_2O]^+$ and 203 $[M+H-C_{10}H_{17}N_3O_6S-H_2O]^+$ were detected in the high-resolution mass spectrum.

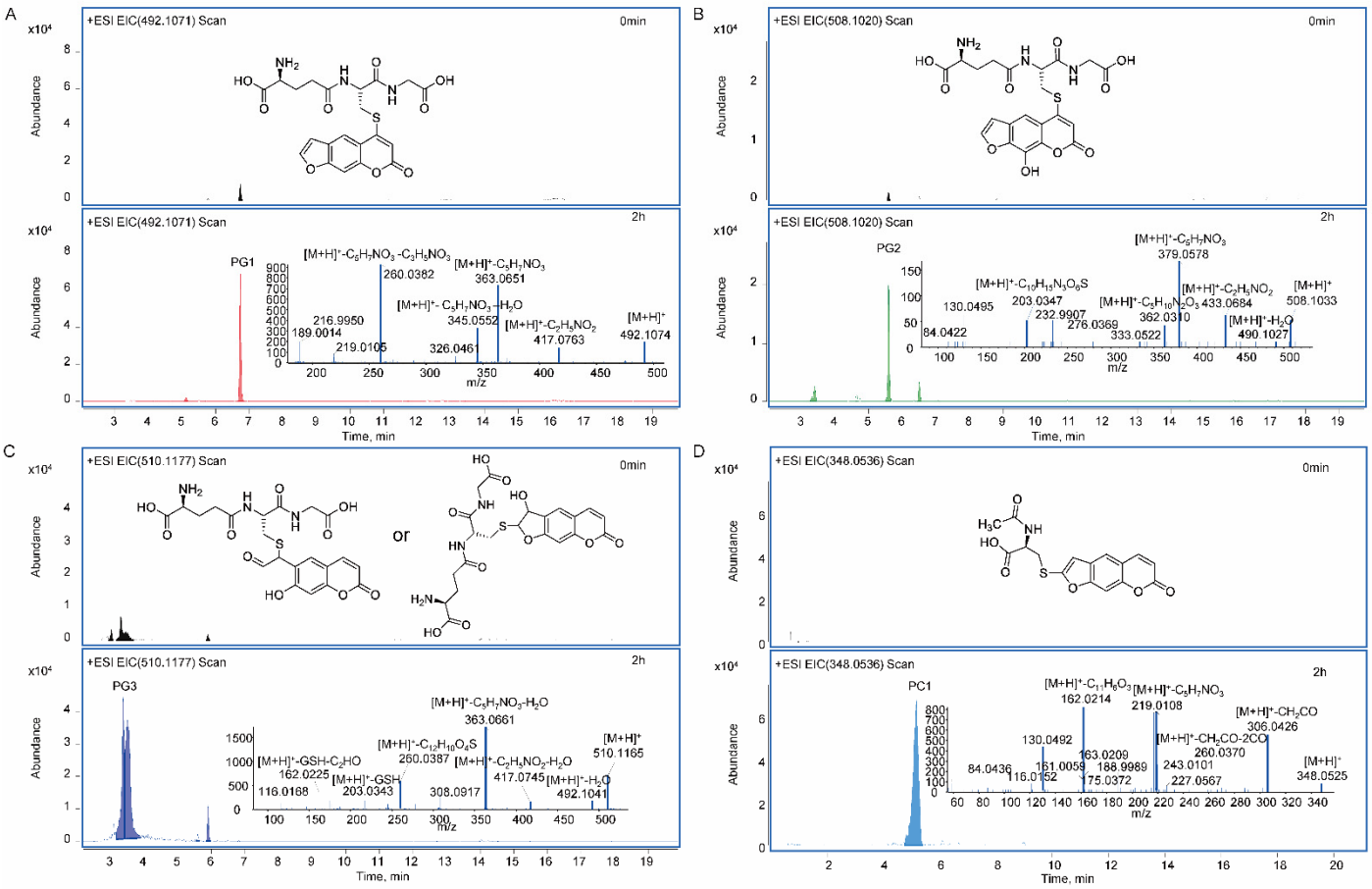

Fig.3 Extracted ion chromatograms (EICs), possible structure of PRN and its RM conjugates with GSH in liver microsome, PG1 (A), PG2 (B), PG3 (C), PC1 (D) and their MS/MS spectrums.

Moreover, three NAC adducts of PRN metabolites, PC1 (Fig.3D), PC2- PC3 (Figs.S7-S8), were first detected from the incubation in RLMs. PC1 displyed a peak at 5.19 min, revealed a molecular ion $[M+H]^+$ at m/z 348.0536, consistent with the elemental formula $C_{16}H_{13}NO_6S$. PC1 generated product ions at m/z 306 $[M+H\text{-}C_2H_2O]^+$, 216 $[M+H\text{-}C_5H_9NO_3]^+$ and 162 $[M+H\text{-}C_{11}H_6O_3]^+$. PC2 and PC3 were identified and showed the $[M+H]^+$ signal at m/z 364.0486, and 366.0642, with a chemical formula of $C_{16}H_{13}NO_7S$ and $C_{16}H_{15}NO_7S$ respectively. They separated at the retention times of 8.56 min and 5.19 min, respectively. PC2 generated the product ions at m/z 322 $[M+H\text{-}C_2H_2O]^+$, 232 $[M+H\text{-}C_5H_9NO_3]^+$ and 130 $[M+H\text{-}C_{11}H_6O_4S]^+$. The main product ions of PC3 were ions at m/z 348 $[M+H\text{-}H_2O]^+$, 203 $[M+H\text{-}C_5H_9NO_3S]^+$ and 175 $[M+H\text{-}C_5H_9NO_3S\text{-}H_2O]^+$, which further manifested that they were NAC conjugates. These results indicate that PRN-RM can covalently bind with cysteine and may covalently modify cysteine residues in proteins.

In addition, the NAL adduct, PL1 (Fig.S9) was first observed and displayed the $[M+H]^+$ signal at m/z 405.1292, with a chemical formula of $C_{19}H_{20}N_2O$. It detected at the retention times of 7.30 min. PL1 generated product ions at m/z 387 $[M+H\text{-}H_2O]^+$, 189 $[M+H\text{-}C_{11}H_4O_5]^+$ and 171 $[M+H\text{-}C_{11}H_4O_5\text{-}H_2O]^+$, which further demonstrated that it was a NAL conjugate. It is significant that the formation of adducts between PRN and NAL has not been documented in prior studies. These findings suggest that PRN metabolites could potentially form adducts with lysine residues in proteins.

3.3 P450 enzymes responsible for bioactivation of PRN

The abovementioned results demonstrated that PRN can undergo metabolism to form PRN RMs-AA adducts. However, the specific metabolic enzymes responsible for this process remain largely unidentified. The study aimed to reveal the individual roles of P450 enzymes in catalyzing the metabolism of PRN by adding specific inhibitors of these enzymes to the GSH capture system previously described. The selection of inhibitors and their respective concentrations was informed by existing literatures and preliminary experiments. The biological activation of CYP enzymes involved in PRN metabolism was investigated through co-incubation with selective CYP enzyme inhibitors, including ketoconazole (CYP3A1), α-naphthoflavone (CYP1A2), sulfaphenazole (CYP2C6), ticlopidine (CYP2C11), quinidine (CYP2D1), disulfiram (CYP2E1), and methoxypsoralen (CYP2A3). Samples containing no inhibitors were included as controls. The results showed that co-incubation with α-naphthoflavone, sulfaphenazole, ketoconazole, ticlopidine, quinidine, disulfiram and methoxypsoralen in microsomes significantly reduced the formation of PG1 (Fig.4A) and PG5 (Fig.4B) ($P < 0.01$), co-incubation with sulfaphenazole, ketoconazole, ticlopidine, disulfiram and methoxypsoralen in microsomes significantly reduced the formation of PG3 (Fig.S10A) ($P < 0.01$), and co-incubation with sulfaphenazole, ketoconazole, quinidine, disulfiram and methoxypsoralen in microsomes significantly reduced the formation of PG6 (Fig.S10B) ($P < 0.01$). This suggests that PRN RMs adducts are likely biologically activated by the corresponding P450 enzymes, particularly CYP2C6, CYP3A1, CYP2E1, and CYP2A3.

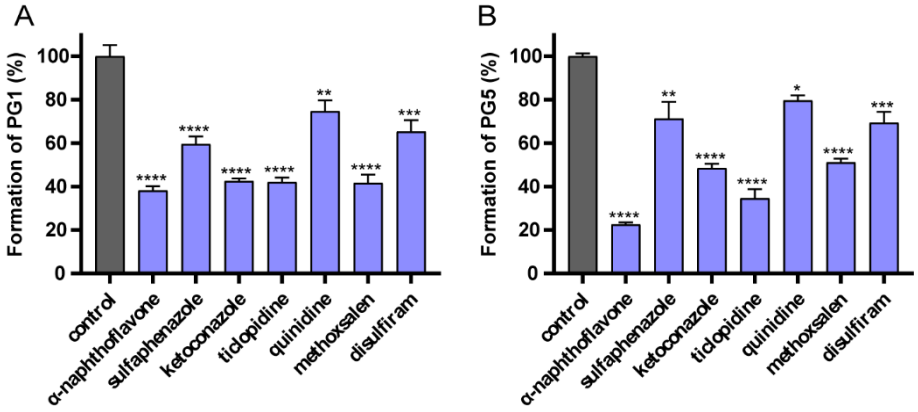

Fig.4 Inhibition effects of P450 inhibitors on the formation of PG1 (A) and PG5 (B) in the RLM incubation system containing NADPH, PRN (20 mmol/L) and GSH (1.0 mmol/L), The concentrations of α-naphthoflavone, sulfaphenylpyrazole, ticlopidine, quinidine, disulfiram, methoxsalen and ketoconazole were 1, 20, 100, 5.0, 100, 100 and 1.0 μmol/L, respectively. Compared with the control group, *$P < 0.05$, **$P < 0.01$, ***$P < 0.001$, ****$P < 0.0001$. Data represent mean ± SEM (n = 3).

3.4 PRN induces hepatotoxicity in vivo

The above studies indicate that PRN is capable of forming adducts through the action of CYP enzymes. Subsequently, we employed KM mice subjected to PRN overdose to assess its hepatotoxic effects. To ascertain whether PRN induces liver damage in these mice, liver function indices were assessed in both control and PRN-treated groups utilizing a specific assay kit. The findings revealed that the serum levels of ALT and AST in the PRN-treated group were elevated in a dose-dependent manner compared to the control group (Fig.5A-B). Additionally, histological analysis through HE staining revealed that, relative to the control

group, the livers of PRN-treated mice displayed significant nuclear pyknosis and lymphocytic infiltration (Fig.5C). These observations confirm that excessive administration of PRN can induce liver injury in mice.

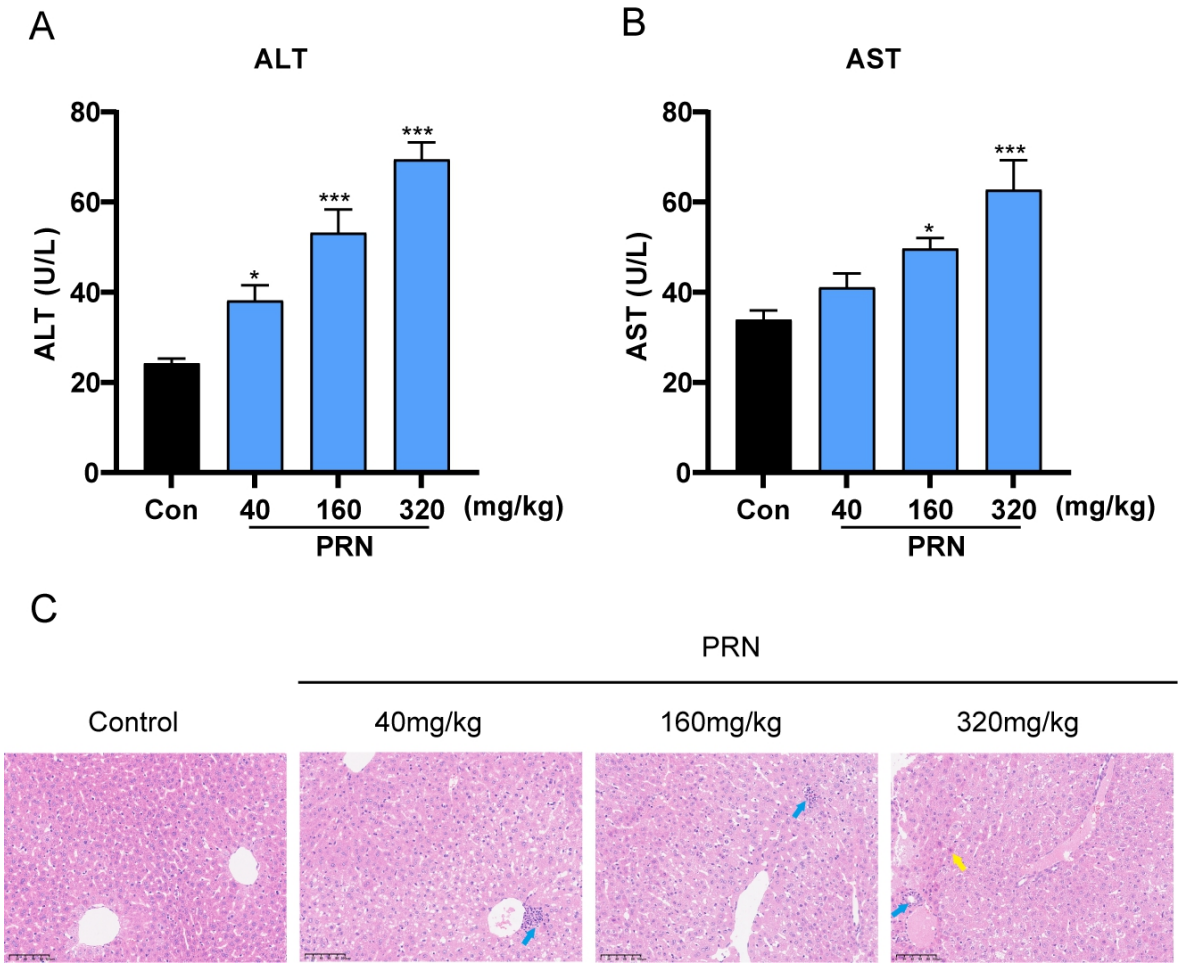

Fig.5 The effect of PRN on liver function *in vivo*. ALT (A), AST (B) levels induced by PRN treatment were detected using activity assay kits in mice. Values expressed as mean ± SD (n ≥ 6) from three independent experiments, **P* < 0.05, ***P* < 0.01, ****P* < 0.001 vs. control group. (C) The histological changes of nuclear pyknosis (yellow arrows) and lymphocytic infiltration (blue arrows) in PRN treated mice were observed (original magnification, ×200). The scale bar is 100 μm.

3.5 Identification of PRN RMs and PRN RMs-AAs adducts in vivo

The above results demonstrated that PRN RMs are capable of covalently binding to model AAs in microsomal systems. We extended our investigation to examine PRN RMs and PRN RMs-AA adducts i*n vivo*. The results showed that PRN RMs (M1-M6) were detectable in the liver of mice treated with PRN. The accurate mass and retention time were consistent with our *in vitro* experimental data. The relative concentrations of the PRN RMs (M1-M6) were quantified by peak areas using LC-MS analysis (Fig.6). The data revealed a significant dose-dependent increase in the content of M1-M6 in PRN-treated mice liver compared to the control group ($P < 0.05$).

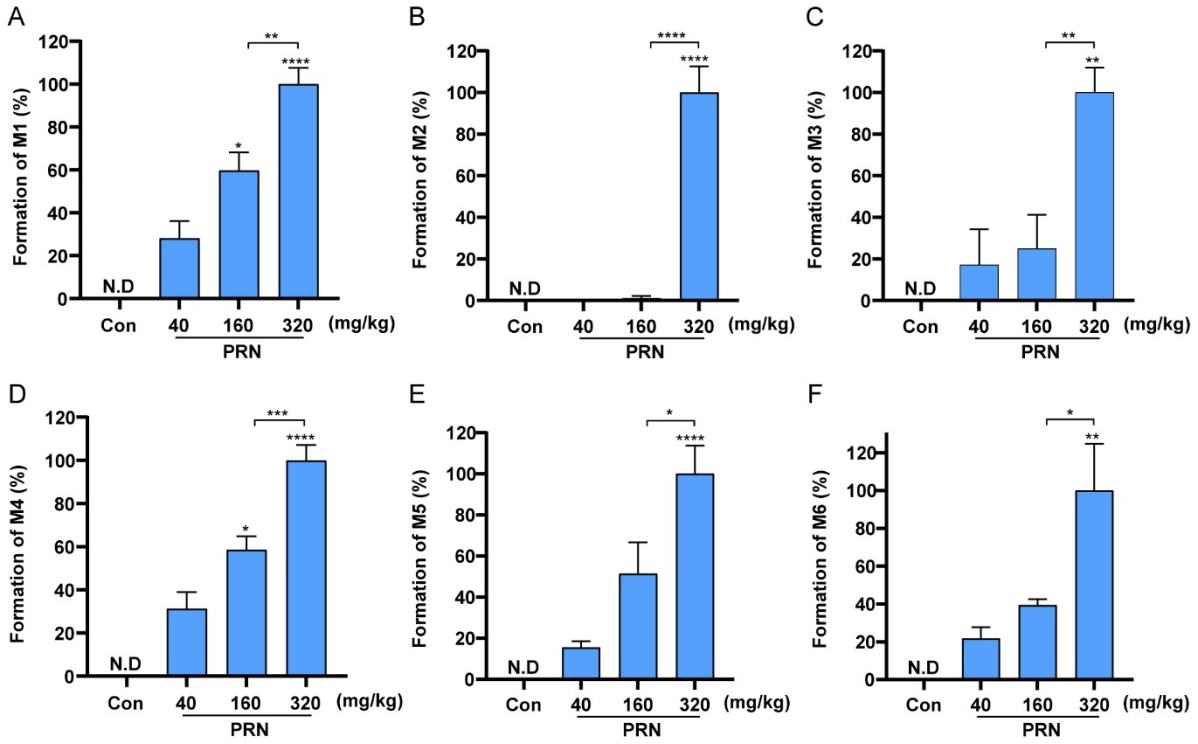

Fig.6 M1 (A), M2 (B), M3 (C), M4 (D), M5 (E), M6 (F) formed in the mice liver of PRN treatment group. Significant difference from the control group, *$P < 0.05$, **$P < 0.01$, ***$P < 0.001$. Data represent mean ± SEM (n ≥ 6).

To determine whether PRN RMs can form adducts with free AAs in mice, the covalent bindings between PRN RMs and free AA in liver were further conducted. The findings revealed that the adducts PG4 and PG6-1, previously detected *in vitro*, were also present *in vivo* (Fig.7). Additionally, two novel adducts of PRN RMs with cysteine (Pcys1, Pcys2) and one novel adduct with lysine (Plys1) were identified (Table 2). The results demonstrated a marked increase of these adducts in the liver of PRN-treated mice (P <0.05) in a dose-dependent manner, which showed that PRN RMs can covalently modify free AAs in mice.

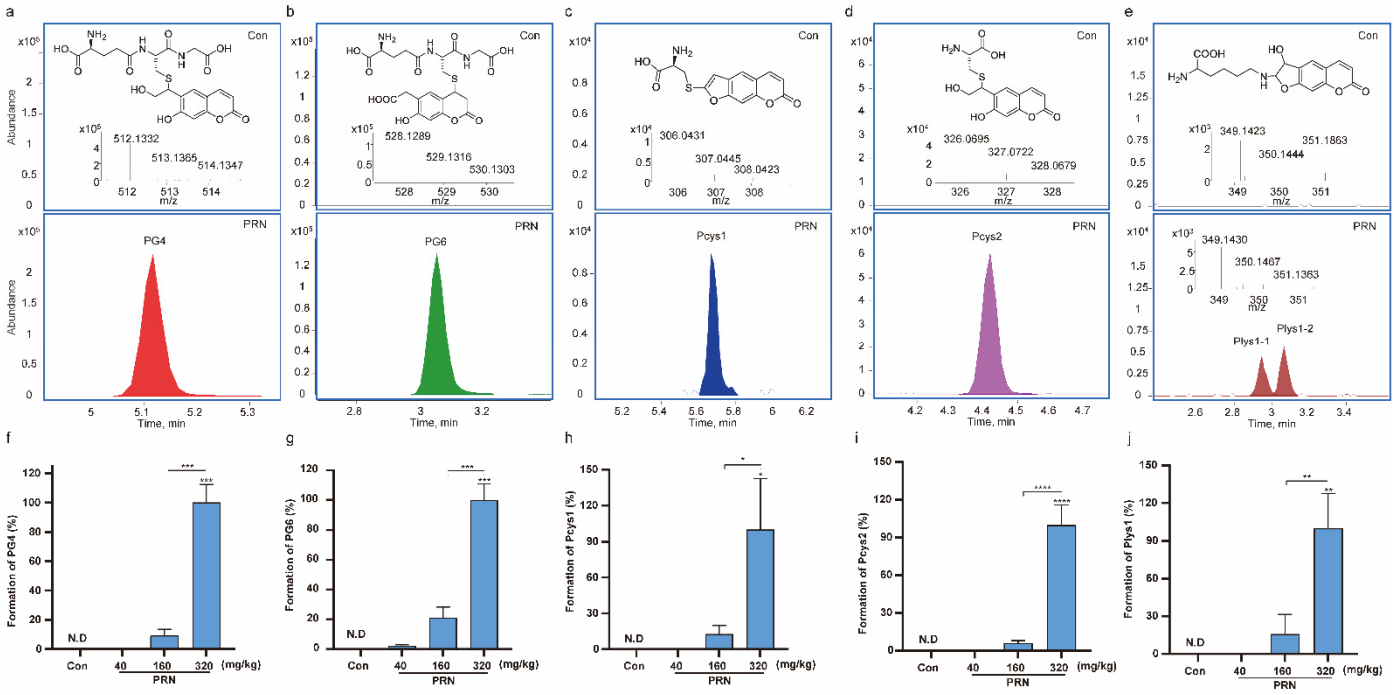

Fig.7 EIC and possible structures of PG4 (A), PG6-1 (B), Pcys1 (C), Pcys2 (D) and Plys1 (E) in liver tissue. Compared with the other group, *$P < 0.05$, **$P < 0.01$, ***$P < 0.001$, ****$P < 0.0001$. Data represent mean ± SEM (n ≥ 6).

3.6 PRN RMs covalently bind to mouse liver proteins

The previous results indicated that PRN RMs can form adducts of AAs by CYP enzyme both *in vitro* and vivo, we hypothesized that covalent modification of protein could be a mechanism of liver injury. Thus, to elucidate whether PRN-RM can covalently modify proteins in mice, chemical proteomics analyses were performed. After administration of PRN at 40 mg kg $^{-1}$ to mice, followed by trypsin digestion, the peptides were analyzed through nano-LC-Orbitrap-MS/MS analysis. The MS and MS/MS data collected were entered into Proteome Discoverer to identify peptides. Seven potential PRN RM modification patterns from PRN RM-AA adducts were included as variable modifications in Proteome Discoverer. The findings revealed that 12 PRN RMs modified proteins were identified in the PRN treatment group (Table 3, Fig.8). The quasi-molecular ion $[M+3H]^{3+}$ at m/z 580.6234 matched the adducted peptide of ^{834}LETVTEVIRSCAAK^{847} for Jouberin (AHI1), showing a mass increase of 220 Da relative to the unmodified peptide, indicating the modification of P6-C. The fragmentation ions y8-y9 and y14 showed an increase of 220 Da compared to the unmodified peptide, indicating a modification at cysteine 844. Other ions, y1, b2, b6 and b8, suggested that the peptide was ^{834}LETVTEVIRSCAAK^{847}. Several other proteins, KN motif and ankyrin repeat domain-containing protein 2 (KANK2), NADH dehydrogenase [ubiquinone]1 alpha subcomplex subunit 2 (NDUA2) and BRCA1-associated protein (BRAP), were also modified by PRN RM on cysteine residues (Figs.S11-S13).

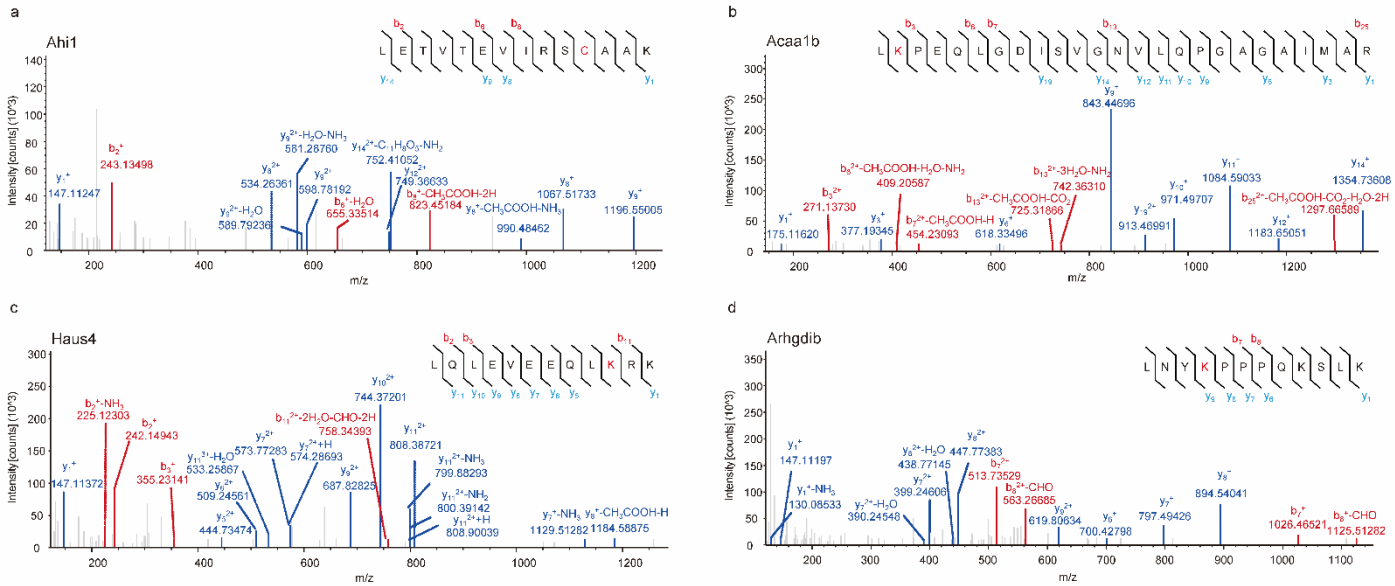

Fig.8 The Representative MS/MS spectra of PRN RM-adducted peptides from Jouberin (Ahi1), 3-ketoacyl-CoA thiolase B, peroxisomal (Acaa1b), HAUS augmin-like complex subunit 4 (Haus4) and Rho GDP-dissociation (Arhgdib) in PRN-treated mouse liver.

Table 3. Identified PRN RM-protein adducts in liver.

No.	UniProt	Full name	Protein	Gene	Molecular Composition of RM	Annotated Sequence	Modification Type	Sequence Positions	Binding Site
1	Q3UNZ2	Gene model 853	Q3UNZ2	Ldc1	$C_{11}H_6O_4$	KSSLDPGGHR	P3-K	306-315	K306
2	Q811L6	Microtubule-associated	MAST4	Mast4	$C_{11}H_6O_4$	KESLERR	P3-K	1255-12	K1255

		serine/threonine-protein kinase 4						61	
3	Q8C0V7	Putative sperm motility kinase W	SMKW	Stk-ps2	$C_{11}H_6O_4$	YNESMGAYLILKAQVDK	P3-K	302-318	K313
4	B1AY15	Ubiquitin carboxyl-terminal hydrolase 51	UBP51	Usp51	$C_{11}H_6O_4$	WFTRPEDLGSSAK	P3-K	506-518	K518
5	Q8VCH0	3-ketoacyl-CoA thiolase B, peroxisomal	THIKB	Acaa1b	$C_{11}H_6O_4$	LKPEQLGDISVGNVLQPGAGAIMAR	P3-K	78-102	K79
6	A2AWL7	MAX gene-associated protein	MGAP	Mga	$C_{11}H_6O_4$	VSSLSGKTEEVVLK	P3-K	2438-2451	K2444
7	Q8BFT2	HAUS augmin-like complex subunit 4	HAUS4	Haus4	$C_{11}H_4O_5$	.LQLEVEEQLKRK	P4-K	164-175	K173
8	Q61599	Rho GDP-dissociation inhibitor 2	GDIR2	Arhgdib	$C_{11}H_4O_5$	.LNYKPPPQKSLK	P4-K	21-32	K24
9	Q8BX02	KN motif and ankyrin repeat domain-containing protein 2	KANK2	Kank2	$C_{11}H_8O_4$	QLLDSGVCHVDKLNR	P7-C	677-691	C684
10	Q8K3E5	Jouberin	AHI1	Ahi1	$C_{11}H_8O_5$	LETVTEVIRSCAAK	P6-C	834-847	C844
11	Q9CQ75	NADH dehydrogenase [ubiquinone]1 alpha subcomplex subunit 2	NDUA2	Ndufa2	$C_{11}H_8O_5$	KAHPNLPILIRECSEVQPK	P6-C	46-64	C58
12	Q99MP8	BRCA1-associated protein	BRAP	Brap	$C_{11}H_8O_5$	TLASAVACLEGK	P6-C	40-51	C47

The liver also showed modifications on lysine residues. For instance, ^{78}LKPEQLGDISVGNVLQPGAGAIMAR^{102} for 3-ketoacyl-CoA thiolase B, peroxisomal (THIKB) displays a quasi-molecular ion $[M+3H]^{3+}$ at m/z 912.7992, which is 202 Da heavier than the unaged peptide, indicating modification by P3-K. The fragmentation ions of b1, b6-b7, b13 and b25 were also increased by 202 Da than the unmodified peptide. Thus, it was proposed that K79 was the binding site. ^{164}LQLEVEEQLKRK^{175} for HAUS augmin-like complex subunit 4 (HAUS4) shows a quasi-molecular ion $[M+3H]^{3+}$ at m/z 576.9645, which is 216 Da heavier than the unaged peptide, showing that the peptide was changed by P4-K. An increase of 216 Da was observed in the fragmentation ions y5-y11 and b11 relative to the unaged peptide, suggesting K173 as the binding site. ^{21}LNYKPPPQKSLK^{32} for Rho GDP-dissociation inhibitor 2 (GDIR2) reveals a quasi-molecular ion $[M+3H]^{3+}$ at m/z 543.6153, which 216 Da more massive than the unaged peptide, indicating it was modified by P4-K. Compared to the unaged peptide, the fragmentation ions of b7-b8 and y9 increased by 216 Da, implying that K24 was the binding site. Likewise, PRN RM modifies lysine residues in Gene model 853 (Q3UNZ2) on K306, Microtubule-associated serine/threonine-protein kinase 4 (MAST4) on K1255, Putative sperm motility kinase W (SMKW) on K313, Ubiquitin carboxyl-terminal hydrolase 51 (UBP51) on K518, and MAX gene-associated protein (MGAP) on K2444 (Table 4. Figs.S14-S18).

Table 4. Binding Energy for proteins with PRN.

Protein	Micromolecule	Binding Energy (kcal/mol)
NDUA2	PRN	-7.139
THIKB	PRN	-5.996

3.7 Label-free quantitative proteomics analysis

To further investigate the mechanism of PRN induced liver injury, LFQ analysis was performed. A total of 8380 proteins were screened in the PRN group. After three replicated biological analyses with high

reliability, a total of 178 differentially expressed proteins (DEPs) were identified between the control group and the PRN group (| log2 (Fold Change) |>1 and $P < 0.05$), of which 74 up-regulated and 104 down-regulated (Fig.9A). The accuracy of the screened differential proteins was verified by cluster analysis. As shown in Fig.9B, the identified differential proteins were significantly different between the two groups, indicating that these DEPs may represent key changes in the liver of mice after PRN administration. Then, to further explore the mechanism of PRN-induced hepatotoxicity, KEGG analysis was done on these DEPs, the results showed that these DEPs are related to Drug metabolism − cytochrome P450, Glutathione metabolism, Thyroid hormone synthesis, Metabolism of xenobiotics by cytochrome P450 (Fig.9C).

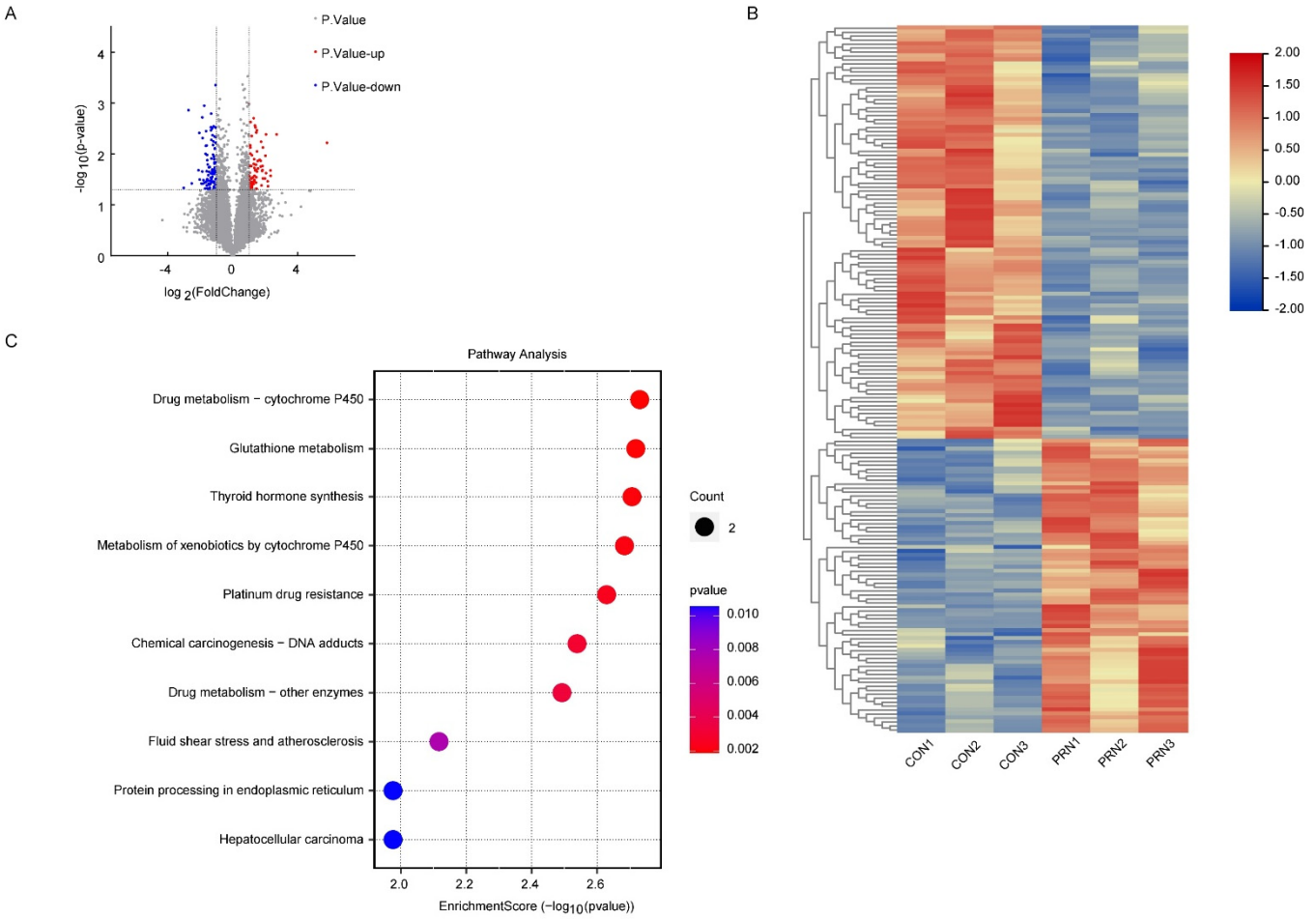

Fig.9 The volcano plot shows the asymmetry between the upregulated (red) and downregulated (blue) differentially expressed proteins identified between the PRN group and the control group (A). Heat map of DEPs between PRN group and control group, the row represents DEP, and the list shows samples with three biological replicates, The signal values of DEPs are displayed as colored bars, with high expression DEPs displayed in red and low expression proteins displayed in blue (B); The KEGG pathway plot of DEPs of PRN vs Control (C).

3.8 The impact of PRN on oxidative stress

We further examined the effect of PRN on oxidative stress *in vivo*. The significant decrease of GSH after exposure (middle and high dosages) showed that PRN impaired the primary antioxidant system against free radicals (Fig.10D). Furthermore, MDA levels, an indicator of oxidative stress, showed a significant increase ($P < 0.05$) following PRN exposure compared to the controls (Fig.10A). The findings showed that PRN treatment increased the production of reactive oxygen species (ROS), which exhausted the antioxidant

defense system and caused lipid peroxidation. SOD activity showed a significant reduction ($P < 0.05$) (Fig.10B), while CAT and GST activities decreased by 24.08 and 16.26%, respectively, following PRN exposure compared to the control group (Fig.10C, Fig.10E).

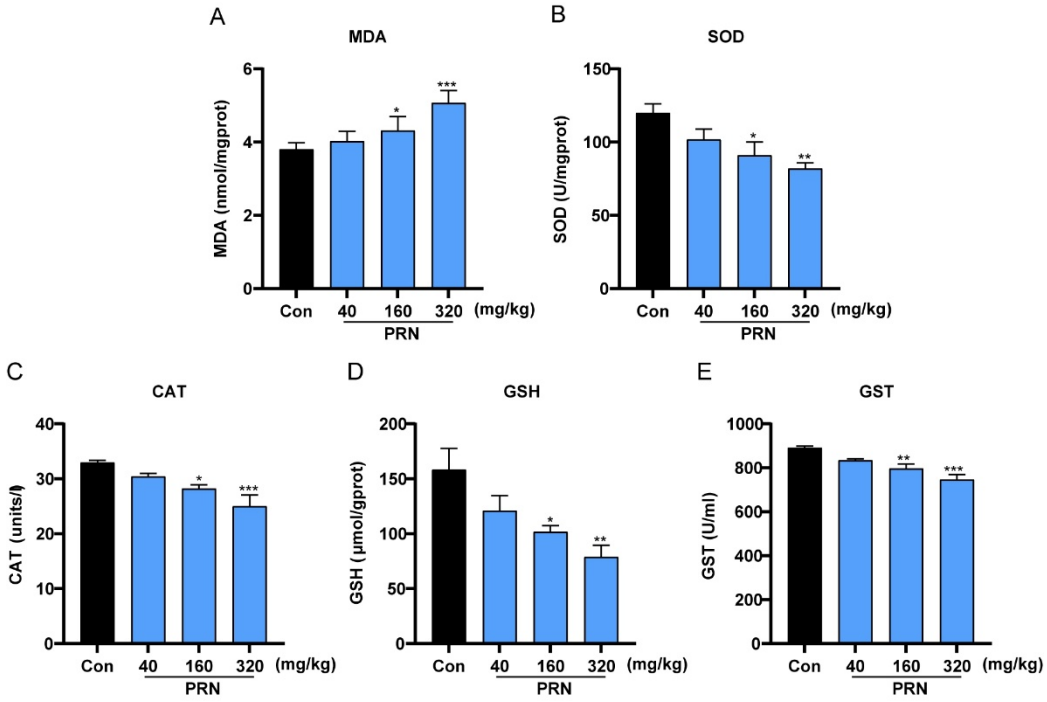

Fig.10 The effect of PRN on oxidative stress, *in vivo*. MDA (A), SOD (B), CAT (C), GSH (D), GST (E), compared with the control group, *$P < 0.05$, **$P < 0.01$, ***$P < 0.001$.

4. Discussion

Furocoumarins, characterized by a reactive furan ring, exhibit biological activity through the ring's reactivity, enabling metabolic activation to form electrophilic intermediates like cis-butene-1,4-dial (BDA) that interact with cellular macromolecules. This study established a mechanism-based approach to screen proteins targeted by furanocoumarins based on reactive metabolites and protein adducts, using the prototypical furanocoumarins PRN as a model compound. *In vitro* incubation systems, identified six PRN-derived RMs (M1-M6) and their adducts with model amino acids (GSH, NAC, NAL). These adducts include PG1-PG6, PC1-PC3, and PL1. Notably, NAC and NAL conjugates were identified for the first time, thereby providing valuable insights into PRN's metabolic pathways and potential for protein modification. In *vivo* investigations identified all PRN RMs (M1-M6) within murine hepatic tissues. A comparative analysis of metabolites in rat liver microsomes and mouse liver showed similar metabolic behavior of PRN in both species, aligning with previous reports [34] . Additionally, *in vivo* detection of PRN RM-amino acid adducts with free amino acids, such as GSH, cysteine, and lysine, was achieved, including PG4, PG6, Acys1, Acys2, and Alys1. Moreover, the formation of BDA as a reactive intermediate is not exclusive to PRN but is also observed in other furan-containing compounds. For instance, the bioactivation of marrubiin, a furanoid compound, involves its conversion to a cis-butene-1,4-dial intermediate, subsequently trapped by nucleophiles such as GSH and NAL [35]. Similarly, rutaevin, another compound with a furan ring, undergoes bioactivation to form a BDA intermediate, which is likewise sequestered by GSH and other nucleophiles [36].

Despite the natural origin, emerging toxicological evidence reveals that some of the furanocoumarins exhibit toxic properties. Imperatorin, a representative furocoumarin, demonstrates organ toxicity in murine models at concentrations as low as 40 mg/kg [37]. Structural analogs such as PRN [25], isopsoralen [38], 8-methoxypsoralen [39], 5-methoxypsoralen [39], and aflatoxin [40] share similar toxicological profiles. Furocoumarin contains a reactive furan ring - a recognized structural alert capable of metabolic activation to electrophilic BDA intermediates [28]. This is particularly relevant in the context of dietary exposure to furan-containing foods, where the formation of BDA and its subsequent reactions can pose health risks [41] Therefore, it is crucial to explore strategies to mitigate the levels of furan and its reactive intermediates in foods to enhance food safety and protect public health. Experimental findings demonstrate that typical furanocoumarin compound PRN significantly elevated the levels of hepatic injury biomarkers (ALT/AST) and induced systemic oxidative stress in mice, with histopathological analysis via HE staining revealing characteristic hepatocellular damage (Fig.5). Crucially, the hepatic accumulation of the specific adducts modified by PRN RMs *in vivo* exhibited dose-dependent increases, which correlated with patterns of ALT/AST elevation (Figs.6-7), thereby establishing a direct relationship between RM formation and hepatic injury. These RMs exhibit covalent binding potential toward nucleophilic protein residues, a well-established mechanism associated with drug-induced liver injury [42]. Building on established methodologies for hepatotoxicity mechanism investigation [19-21], this work systematically explored PRN's bioactivation pathways and subsequent protein interactions.

Drug metabolism activation is typically mediated by the cytochrome P450 family [43]. For instance, CYP3A, primarily present in the liver, accounts for approximately 30% of total hepatic P450 enzymes and is responsible for the metabolism of most drugs [44]. Furocoumarins undergo metabolic activation via cytochrome P450 enzymes, resulting in the formation of reactive intermediates like furanoepoxide or γ-ketoenal. The reactive intermediates can inhibit CYP3A4, a pivotal enzyme in drug metabolism [45]. Such inhibition may lead to food-drug interactions and contribute to the hepatotoxic potential of furocoumarins -containing foods and medicinal herbs. In this study, the enzymatic inhibition investigation revealed predominant roles for CYP2C6, CYP3A1, CYP2E1, and CYP2A3 in PRN RMs-AA adducts generation. These enzymes play crucial roles in maintaining normal liver function, the bioactivation mediated by cytochrome P450 emerged as a critical determinant of PRN hepatotoxicity [21] [46].

Current research suggests that drugs-RMs covalently bound to proteins typically lead to acute liver toxicity [19, 47, 48] Expanding on reported associations between PRN RMs-adducts and hepatotoxicity [25], our chemical proteomics techniques identified 12 distinct PRN RMs-protein adducts. Notably, NDUA2 (Ndufa2), as a key subunit of NADH dehydrogenase, was found to be one of the main modification targets of PRN RMs. This protein is crucial for transferring electrons from NADH to the respiratory chain [49] . This interaction may impair NADPH homeostasis - a key regulator of glutathione redox cycling (GSH/GSSG) and cysteine reduction [50]. Given that GSH is a crucial antioxidant in cells, it assists in maintaining proteins in the reduced state [51]. Further studies have shown that PRN protein modification has a significant effect on GSH metabolic

network. LFQ quantitative proteomics suggested that these DEPs were associated with GSH metabolism (Fig.9). Experimental data showed that GSH content in liver of PRN treatment group showed a significant dose-dependent decrease (Fig.10D). GSH is an essential antioxidant, protecting cellular components from the effects of oxidative stress and injury. The loss of GSH will disrupt the redox balance and cause reactive oxygen species (ROS) accumulation, eventually triggering cell dysfunction and death [52]. Abnormal accumulation of ROS is confirmed by elevated levels of MDA, a maker of oxidative stress (Fig.10A). Additionally, the activity of SOD and CAT, the key antioxidant enzymes forming the primary intracellular defense against ROS [53], decreased significantly (Fig.10B-C). Lowered antioxidant enzymes activities increase the susceptibility of liver to oxidative damage. Furthermore, we propose that the covalent modification of NDUA2, a core subunit of mitochondrial Complex I[54], would directly disrupt the mitochondrial electron transport chain, leading to a primary burst of mitochondria-derived ROS (mtROS) [55]. This excessive mtROS could simultaneously activate the compensatory KEAP1-NRF2 antioxidant pathway [56, 57]. Another modified protein BRAP is a known negative regulator of NRF2, which constrains its nuclear translocation under homeostatic conditions [58]. We hypothesize that BRAP modification leads to aberrant NRF2 activation, ultimately resulting in an exhaustion of this vital antioxidant pathway, leaving the cell vulnerable to subsequent oxidative damage. Thus, the covalent modification of key targets (NDUA2 and BRAP) by PRN RMs could result in the dysregulation of the NRF2 pathway, and resulting the escalation of oxidative stress. While the present study provides strong associative evidence, direct functional validation of the roles of NDUA2, BRAP, and the NRF2 pathway will be a crucial focus of our future research. Thus, integrative analysis supports a triphasic hepatotoxicity mechanism: (1) RM-protein adduct formation, (2) GSH metabolic dysregulation, and (3) oxidative stress cascade. This progression from molecular modification to systemic redox collapse provides a mechanistic framework for PRN-induced liver injury, advancing our understanding of furanocoumarin toxicity.

5. Conclusion

In conclusion, the newly established LC-MS-based analytical strategy for RMs and protein adducts has systematically elucidated the potential food-drug interactions and hepatotoxicity mechanism of furanocoumarin compounds through a comprehensive multi-dimensional approach. Initially, the intrinsic hepatotoxicity of furanocoumarins was confirmed. Subsequently, an *in vitro* microsomal incubation system, integrated with LC-MS analysis, was utilized to characterize their metabolic activation patterns and amino acid modification profiles. This was further complemented by CYP inhibition assays to identify the primary metabolic enzymes involved. Additionally, *in vivo* experiments demonstrated that free AAs in the liver can covalently modify the RMs of furanocoumarins. Concurrently, specific target proteins covalently modified by furanocoumarin RMs were identified using chemical proteomics approaches. Finally, an integrative analysis combining quantitative proteomics and biological validation elucidated the molecular mechanisms underlying furanocoumarin-induced hepatotoxicity. Through this strategy, PRN, a representative furanocoumarin, induces liver injury via P450-mediated generation of electrophilic intermediates that: (1) form stable adducts

with critical proteins (e.g., Ndufa2), thereby disrupting cellular energetics; (2) deplete glutathione reserves, impairing redox homeostasis; (3) initiate oxidative stress cascades that culminate in hepatocellular damage; and (4) CYPs were the primary enzymes responsible for forming PRN RM-protein adducts, this process can influence drug metabolism and potentially cause food-drug interactions. This investigation establishes a mechanistic framework that links furanocoumarin bioactivation to food-drug interactions and hepatotoxicity through an integrative analysis of RMs, covalent protein adducts, and pathway perturbations. It provides a template for elucidating potential dual role of food-drug interactions and hepatotoxicity mechanisms induced by furanocoumarin-containing food, emphasizing the importance of identifying structural alerts and assessing metabolic activation potential in the safety evaluation natural products.

Data availability statement

The mass spectrometry proteomics data have been deposited to the ProteomeXchange Consortium via the PRIDE partner repository with the dataset identifier PXD064256.

Funding

This work was supported by the funding from National Natural Science Foundation of China (No. 82405200) and Guangzhou Municipal Science and Technology Bureau (2024A04J4900).

Declaration of competing interest

The authors declare that there are no conflicts of interest.

References

[1] S. Gong, G. Bai, Y. Ban, et al., The underappreciated diversity of furanocoumarins in grapefruits revealed by MassQL filtered molecular networking, FoodChem. X 25 (2025) 102233. https://doi.org/10.1016/j.fochx.2025.102233.

[2] J. Cao, L. Zheng, L. Ji, et al., Mechanism-based inactivation of cytochrome P450 2B6 by isoimperatorin, Chem. Biol. Interact. 226 (2015) 23-29. https://doi.org/10.1016/j.cbi.2014.12.009.

[3] X.Y. Zhang, X.J. Liao, Y.T. Wang, et al., Health effects of fruit juices and beverages with varying degrees of processing, Food. Sci. Hum. Well. 13 (2024) 2456-2479. https://doi.org/10.26599/Fshw.2022.9250202.

[4] X.M. Lu, C.Y. Zhao, H. Shi, et al., Nutrients and bioactives in citrus fruits: different citrus varieties, fruit parts, and growth stages, Crit. Rev. Food. Sci. Nutr. 63 (2023) 2018-2041. https://doi.org/10.1080/10408398.2021.1969891.

[5] W.L. Hung, J.H. Suh, Y. Wang, Chemistry and health effects of furanocoumarins in grapefruit,J. Food Drug Anal. 25 (2017) 71-83. https://doi.org/10.1016/j.jfda.2016.11.008.

[6] J.L. Rodrigues, L.R. Rodrigues, Biosynthesis and heterologous production of furanocoumarins: perspectives and current challenges, Nat. Prod. Rep. 38 (2021) 869-879. https://doi.org/10.1039/d0np00074d.

[7] M.M. Melough, O.K. Chun, Dietary furocoumarins and skin cancer: a review of current biological evidence, Food. Chem. Toxicol. 122 (2018) 163-171. https://doi.org/10.1016/j.fct.2018.10.027.

[8] S. Ahmed, H. Khan, M. Aschner, et al., Anticancer potential of furanocoumarins: mechanistic and therapeutic aspects, Int. J. Mol. Sci. 21 (2020) 5622. https://doi.org/10.3390/Ijms21165622.

[9] J.F. Yan, H. Hirao, QM/MM study of the metabolic oxidation of 6′,7′-dihydroxybergamottin catalyzed by human CYP3A4: preferential formation of the γ-ketoenal product in mechanism-based inactivation, J. Chem. Inf. Model. 65 (2025) 4620-4629. https://doi.org/10.1021/acs.jcim.5c00259.

[10] M. Tian, Y. Peng, J. Zheng, Metabolic activation and hepatotoxicity of furan-containing compounds, Drug. Metab. Dispos. 50 (2022) 655-670. https://doi.org/10.1124/dmd.121.000458.

[11] S. Berteina-Raboin, Flavonoids and furanocoumarins involved in drug interactions, Molecules 30 (2025) 1676. https://doi.org/10.3390/Molecules30081676.

[12] D.G. Bailey, G. Dresser, J.M. Arnold, Grapefruit-medication interactions: forbidden fruit or avoidable consequences?, CMAJ 185 (2013) 309-316. https://doi.org/10.1503/cmaj.120951.

[13] H. Niu, Aruhan, S. Surenjidiin, et al., Yinshan Zhengyao: exploring the power of food and inheriting healthy thoughts, Food Med. Homol. 1 (2024) 9420006. https://doi.org/10.26599/FMH.2024.9420006.

[14] X.L. Hu, J.W. Liu, J.L. Wu, et al., Chemical proteomics unraveling the contribution of covalent protein modifications to antidepressant effects of ketamine, J. Anal. Test. https://doi.org/10.1007/s41664-025-00369-8 (2025),

[15] M.G. Leeming, W.A. Donald, R.A.J. O'Hair, Nontargeted identification of reactive metabolite protein adducts, Anal. Chem. 89 (2017) 5748-5756. https://doi.org/10.1021/acs.analchem.6b04604.

[16] Y.M. Koen, N.A. Galeva, I.G. Metushi, et al., Protein targets of isoniazid-reactive metabolites in mouse liver in vivo, Chem. Res. Toxicol. 29 (2016) 1064-1072. https://doi.org/10.1021/acs.chemrestox.6b00098.

[17]J. Gan, H. Zhang, W.G. Humphreys, Drug-protein adducts: chemistry, mechanisms of toxicity, and methods of characterization, Chem. Res. Toxicol. 29 (2016) 2040-2057. https://doi.org/10.1021/acs.chemrestox.6b00274.

[18] H. Deng, Q. Lei, Y. Wu, et al., Activity-based protein profiling: recent advances in medicinal chemistry, Eur. J. Med. Chem. 191 (2020) 112151. https://doi.org/10.1016/j.ejmech.2020.112151.

[19] Y. Zhuo, Y. Zhang, M. Li, et al., Hepatotoxic evaluation of toosendanin via biomarker quantification and pathway mapping of large-scale chemical proteomics, Food. Chem. Toxicol. 153 (2021) 112257. https://doi.org/10.1016/j.fct.2021.112257.

[20] Y. Zhuo, J.L. Wu, X. Yan, et al., Strategy for hepatotoxicity prediction induced by drug reactive metabolites using human liver microsome and online 2D-nano-LC-MS analysis, Anal. Chem. 89 (2017) 13167-13175. https://doi.org/10.1021/acs.analchem.7b02684.

[21] H. Chen, C. Liu, M. Li, et al., Ferulic acid prevents diosbulbin b-induced liver injury by inhibiting covalent modifications on proteins, Drug. Metab. Pharmacokinet. 50 (2023) 100507. https://doi.org/10.1016/j.dmpk.2023.100507.

[22] Y. Zhuo, H. Chen, C. Liu, et al., Covalent modification of proteins by osthole reactive metabolites using proteomic approaches, Curr. Drug Metab. 24 (2023) 611-620. https://doi.org/10.2174/1389200224666230727123006.

[23] Z. Milanovic, Exploring enzyme inhibition and comprehensive mechanisms of antioxidant/prooxidative activity of natural furanocoumarin derivatives: a comparative kinetic DFT study, Chem. Biol. Interact. 396 (2024) 111034. https://doi.org/10.1016/J.Cbi.2024.111034.

[24] D. Meng, Y. Dong, Q. Shang, et al., Anti-tumor effect and hepatotoxicity mechanisms of psoralen, Front. Pharmacol. 15 (2024) 1442700. https://doi.org/10.3389/fphar.2024.1442700.

[25] M. Jiang, X. Wang, B. Lv, et al., Psoralen induces hepatotoxicity by covalently binding to glutathione-S-transferases and the hepatic cytochrome P450, Phytomedicine 104 (2022) 154165. https://doi.org/10.1016/j.phymed.2022.154165.

[26] J. Jamalis, F.S.M. Yusof, S. Chander, et al., Psoralen derivatives: recent advances of synthetic strategy and pharmacological properties, Anti-Inflamm. Anti-Allergy Agents Med. Chem. 19 (2020) 222-239. https://doi.org/10.2174/1871523018666190625170802.

[27] I. Amunom, L.J. Dieter, V. Tamasi, et al., Cytochromes P450 catalyze the reduction of α,β-unsaturated aldehydes, Chem. Res. Toxicol. 24 (2011) 1223-1230. https://doi.org/10.1021/tx200080b.

[28] Y. Hai, S. Feng, L. Wang, et al., Coordination mechanism and bio-evidence: reactive γ-ketoenal intermediated hepatotoxicity of psoralen and isopsoralen based on computer approach and bioassay, Molecules 22 (2017) 1451. https://doi.org/10.3390/molecules22091451.

[29] Y. Lu, M. Zhang, J. Zhang, et al., Psoralen prevents the inactivation of estradiol and treats osteoporosis via covalently targeting HSD17B2, J. Ethnopharmacol. 311 (2023) 116426. https://doi.org/10.1016/j.jep.2023.116426.

[30] C. Gao, C. Liu, Y. Wei, et al., The acute oral toxicity test of ethanol extract of salt-processed psoraleae fructus and its acute hepatotoxicity and nephrotoxicity risk assessment, J. Ethnopharmacol. 309 (2023) 116334. https://doi.org/10.1016/j.jep.2023.116334.

[31] Y. Wang, H. Zhang, J.M. Jiang, et al., Hepatotoxicity induced by psoralen and isopsoralen from fructus psoraleae: wistar rats are more vulnerable than ICR mice, Food. Chem. Toxicol. 125 (2019) 133-140. https://doi.org/10.1016/j.fct.2018.12.047.

[32] Y.J. Zhang, W.L. Zhou, F. Yu, et al., Evaluation of the effect of bovis calculus artifactus on eight rat liver cytochrome P450 isozymes using LC-MS/MS and cocktail approach, Xenobiotica 51 (2021) 1010-1018. https://doi.org/10.1080/00498254.2021.1959673.

[33] C. Liu, X. Zhuo, F.J. Gonzalez, et al., Baculovirus-mediated expression and characterization of rat CYP2A3 and human CYP2a6: role in metabolic activation of nasal toxicants, Mol. Pharmacol.. 50 (1996) 781-788.

[34] A. Yang, J. Chen, Y. Ma, et al., Studies on the metabolites difference of psoralen/isopsoralen in human and six mammalian liver microsomes in vitro by UHPLC-MS/MS, J. Pharm. Biomed. Anal. 141 (2017) 200-209. https://doi.org/10.1016/j.jpba.2017.04.026.

[35] Y.T. Xing, H. Xing, Y.C. Ma, et al., In vitro and In vivo studies of metabolic activation of marrubiin, a bioactive constituent from marrubium vulgare, Chem. Res. Toxicol. 34 (2021) 2157-2165. https://doi.org/10.1021/acs.chemrestox.1c00250.

[36] Y.T. Liu, C. Liu, Y.M. Liu, et al., Cytochrome P450 mediated bioactivation of rutaevin, a bioactive and potentially hepatotoxic component of evodia rutaecarpa, Chem. Res. Toxicol. 33 (2020) 3054-3064. https://doi.org/10.1021/acs.chemrestox.0c00475.

[37] H. Deng, Q. Lei, Y.P. Wu, et al., Activity-based protein profiling: recent advances in medicinal chemistry, Eur. J. Med. Chem. 191 (2020) 112151. https://doi.org/10.1016/J.Ejmech.2020.112151.

[38] Y. Wang, Q. Zhou, H. Wang, et al., Effect of P. corylifolia on the pharmacokinetic profile of tofacitinib and the underlying mechanism, Front. Pharmacol. 15 (2024) 1351882. https://doi.org/10.3389/fphar.2024.1351882.

[39] Z. Alehaideb, M. Sheriffdeen, F.C.P. Law, Inhibition of caffeine metabolism by apiaceous and rutaceae families of plant products in humans: in vivo and in vitro studies, Front. Pharmacol. 12 (2021) 641090. https://doi.org/10.3389/fphar.2021.641090.

[40] E.H. Branstad-Spates, C.S. McCarthy, B.C. Dooley, et al., Supplementing silicoglycidol for the reduction of aflatoxin M(1) in milk and biomarkers of liver dysfunction in dairy cows, JDS. Commun. 5 (2024) 684-689. https://doi.org/10.3168/jdsc.2023-0538.

[41] Y.J. Zhang, Y. Zhang, A comprehensive review of furan in foods: from dietary exposures and in vivo metabolism to mitigation measures, Compr. Rev. Food Sci. Food Saf. 22 (2023) 809-841. https://doi.org/10.1111/1541-4337.13092.

[42] A.F. Stepan, D.P. Walker, J. Bauman, et al., Structural alert/reactive metabolite concept as applied in medicinal chemistry to mitigate the risk of idiosyncratic drug toxicity: a perspective based on the critical examination of trends in the top 200 drugs marketed in the United States, Chem. Res. Toxicol. 24 (2011) 1345-1410. https://doi.org/10.1021/tx200168d.

[43] A. Potęga, M. Kosno, Z. Mazerska, Novel insights into conjugation of antitumor-active unsymmetrical bisacridine C-2028 with glutathione: characteristics of non-enzymatic and glutathione S-transferase-mediated reactions, J. Pharm. Anal. 11 (2021) 791-798. https://doi.org/10.1016/j.jpha.2021.03.014.

[44] J.J. Wang, J.J. Guo, J. Zhan, et al., An in-vitro cocktail assay for assessing compound-mediated inhibition of six major cytochrome P450 enzymes, J. Pharm. Anal. 4 (2014) 270-278. https://doi.org/10.1016/j.jpha.2014.01.001.

[45] Y. Hai, S. Feng, L.L. Wang, et al., Coordination mechanism and bio-evidence: reactive γ-ketoenal intermediated hepatotoxicity of psoralen and isopsoralen based on computer approach and bioassay, Molecules 22 (2017) 1451. https://doi.org/10.3390/Molecules22091451.

[46] M. Zhao, J. Ma, M. Li, et al., Cytochrome P450 enzymes and drug metabolism in Humans, Int. J. Mol. Sci. 22 (2021) 12808. https://doi.org/10.3390/ijms222312808.

[47] X.L. Hu, J.L. Wu, Q. He, et al., Strategy for cysteine-targeting covalent inhibitors screening using in-house database based LC-MS/MS and drug repurposing, J. Pharm. Anal. 24 (2024) 101045. https://doi.org/10.1016/j.jpha.2024.101045.

[48] Z. Li, Q. Fan, M. Chen, et al., The interaction between polyphyllin I and SQLE protein induces hepatotoxicity through SREBP-2/HMGCR/SQLE/LSS pathway, J. Pharm. Anal. 13 (2023) 39-54. https://doi.org/10.1016/j.jpha.2022.11.005.

[49] I. Vercellino, L.A. Sazanov, SCAF1 drives the compositional diversity of mammalian respirasomes, Nat. Struct. Mol. Biol. 31 (2024) 1061-1071. https://doi.org/10.1038/s41594-024-01255-0.

[50] X. Fang, J. Zhang, Y. Li, et al., Malic enzyme 1 as a novel anti-ferroptotic regulator in hepatic ischemia/reperfusion injury, Adv. Sci. 10 (2023) e2205436. https://doi.org/10.1002/advs.202205436.

[51] F. Xie, Y. Niu, X. Chen, et al., Ursodeoxycholic acid inhibits the uptake of cystine through SLC7A11 and impairs de novo synthesis of glutathione, J. Pharm. Anal. 15 (2025) 101068. https://doi.org/10.1016/j.jpha.2024.101068.

[52] C. Bai, J. Liu, L. Bai, et al., Design of a nanozyme-based magnetic nanoplatform to enhance photodynamic therapy and immunotherapy, J. Pharm. Anal. 14 (2024) 100928. https://doi.org/10.1016/j.jpha.2023.12.018.

[53] M.K. Trivedi, P. Panda, K.K. Sethi, et al., Solid and liquid state characterization of tetrahydrocurcumin using XRPD, FT-IR, DSC, TGA, LC-MS, GC-MS, and NMR and its biological activities, J. Pharm. Anal. 10 (2020) 334-345. https://doi.org/10.1016/j.jpha.2020.02.005.

[54] S. Park, J.A. Trujillo-Hernandez, R.L. Levine, Ndufaf2, a protein in mitochondrial complex I, interactswith methionine sulfoxide reductases, Redox. Rep. 28 (2023) https://doi.org/10.1080/13510002.2023.2168635.

[55] Y.C. Sun, X.H. Yuan, W.L. Huang, et al., Fuzheng Huayu recipe inhibits alveolar macrophage M2 polarization and oxidative phosphorylation via METTL3-mediated NDUFA2 m6A modification, J. Bioenerg. Biomembr. (2025) https://doi.org/10.1007/s10863-025-10074-x.

[56] X.S. Jiang, M.Y. Cai, X.J. Li, et al., Activation of the Nrf2/ARE signaling pathway protects against palmitic acid-induced renal tubular epithelial cell injury by ameliorating mitochondrial reactive oxygen species-mediated mitochondrial dysfunction, Front. Med. 9 (2022) 939149. https://doi.org/10.3389/Fmed.2022.939149.

[57] C.F. Liu, M. Rokavec, Z.K. Huang, et al., Curcumin activates a ROS/KEAP1/NRF2/miR-34a/b/c cascade to suppress colorectal cancer metastasis, Cell Death Differ. 30 (2023) 1771-1785. https://doi.org/10.1038/s41418-023-01178-1.

[58] Q. Hu, D.R. D'Amora, L.T. MacNeil, et al., The oxidative stress response in caenorhabditis elegans Requires the GATA Transcription Factor ELT-3 and SKN-1/Nrf2, Genetics 206 (2017) 1909-1922. https://doi.org/10.1534/genetics.116.198788.